

# Higgs Physics: Theory, Experiment and the Future

Sheersh Sen, Hamsini N S, and Anirudhya Pramanik  
*Indian Institute of Science*

We present an overview of the theoretical foundations of the Higgs mechanism, responsible for electroweak symmetry breaking along with the current experimental status of the Higgs boson measurements. An emphasis is placed on the search for the Higgs and methods employed to probe its properties. Finally, the impact of measurements in the Higgs sector on theoretical developments beyond the standard model are explored, along with analysis techniques for Higgs measurements in the purview of the standard model.

## CONTENTS

<p>Introduction <span style="float: right;">2</span></p> <p>I. Theoretical Framework <span style="float: right;">2</span></p> <p style="padding-left: 20px;">A. Goldstone's Theorem and Its Limitations in Gauge Theories <span style="float: right;">2</span></p> <p style="padding-left: 20px;">B. The Higgs Mechanism <span style="float: right;">3</span></p> <p style="padding-left: 40px;">1. Higgs Mechanism in Electroweak Theory <span style="float: right;">3</span></p> <p style="padding-left: 20px;">C. Mass Generation and Boson Mixing <span style="float: right;">3</span></p> <p style="padding-left: 20px;">D. Higgs Potential <span style="float: right;">4</span></p> <p style="padding-left: 40px;">1. Oscillations in the Higgs Potential <span style="float: right;">4</span></p> <p style="padding-left: 40px;">2. Equations of Motion for Fluctuations <span style="float: right;">4</span></p> <p style="padding-left: 20px;">E. Spontaneous Symmetry Breaking in Non-Abelian Theories <span style="float: right;">5</span></p> <p style="padding-left: 40px;">1. SU(3) Example: Scalars in the Octet Representation <span style="float: right;">5</span></p> <p style="padding-left: 40px;">2. Structure of Vector Boson Masses <span style="float: right;">5</span></p> <p style="padding-left: 40px;">3. Residual Unbroken Symmetry <span style="float: right;">5</span></p> <p style="padding-left: 40px;">4. Implications for Electroweak Symmetry Breaking <span style="float: right;">5</span></p> <p style="padding-left: 40px;">5. Incomplete Multiplets <span style="float: right;">5</span></p> <p style="padding-left: 20px;">F. Generalization to Composite Higgs Models <span style="float: right;">5</span></p> <p style="padding-left: 20px;">G. Experimental Confirmation and Open Questions <span style="float: right;">5</span></p> <p style="padding-left: 20px;">H. Mass Constraint on the Higgs Boson <span style="float: right;">5</span></p> <p style="padding-left: 40px;">1. Higgs Sector Possibilities <span style="float: right;">5</span></p> <p style="padding-left: 40px;">2. Higgs Mass Constraints <span style="float: right;">6</span></p> <p style="padding-left: 40px;">3. Theoretical Constraints <span style="float: right;">6</span></p> <p style="padding-left: 40px;">4. Renormalization Group Constraints <span style="float: right;">6</span></p> <p style="padding-left: 40px;">5. Running of Yukawa Couplings <span style="float: right;">6</span></p> <p style="padding-left: 40px;">6. Triviality Bound on <math>M_H</math> <span style="float: right;">6</span></p> <p style="padding-left: 20px;">I. The Problem Without the Higgs Mechanism <span style="float: right;">8</span></p> <p style="padding-left: 20px;">J. Naturalness and the Higgs Boson in the Standard Model <span style="float: right;">8</span></p> <p style="padding-left: 40px;">1. Fermion Loop Corrections (Top Quark Contribution) <span style="float: right;">8</span></p> <p style="padding-left: 40px;">2. Gauge Boson Loop Corrections <span style="float: right;">8</span></p> <p style="padding-left: 40px;">3. Higgs Self-Interaction Corrections <span style="float: right;">9</span></p> <p style="padding-left: 20px;">K. Feynman Rules <span style="float: right;">9</span></p> <p>II. Higgs decays and interactions <span style="float: right;">10</span></p> <p style="padding-left: 20px;">A. Decay to Fermions: <span style="float: right;">10</span></p> <p style="padding-left: 20px;">B. Including QCD (strong force) effects: <span style="float: right;">10</span></p> <p style="padding-left: 20px;">C. Why mostly <math>h \rightarrow b\bar{b}</math> decay? <span style="float: right;">10</span></p>	<p style="padding-left: 20px;">D. Higgs decay to weak Bosons (W,Z): <span style="float: right;">10</span></p> <p style="padding-left: 20px;">E. Gluons: <span style="float: right;">11</span></p> <p style="padding-left: 20px;">F. Dominant Contribution: <span style="float: right;">11</span></p> <p style="padding-left: 20px;">G. Photons: <span style="float: right;">11</span></p> <p style="padding-left: 20px;">H. Loop Functions: <span style="float: right;">12</span></p> <p>III. Search for the Higgs boson <span style="float: right;">12</span></p> <p style="padding-left: 20px;">A. Difficulties involved in Higgs boson searches <span style="float: right;">12</span></p> <p style="padding-left: 20px;">B. Pre-LEP Searches <span style="float: right;">13</span></p> <p style="padding-left: 20px;">C. LEP1 Period <span style="float: right;">13</span></p> <p style="padding-left: 40px;">1. Production Mechanisms at the Z Resonance <span style="float: right;">13</span></p> <p style="padding-left: 40px;">2. Low-Mass Searches <span style="float: right;">14</span></p> <p style="padding-left: 20px;">D. LEP2 Period <span style="float: right;">15</span></p> <p style="padding-left: 40px;">1. Signal Characteristics <span style="float: right;">15</span></p> <p style="padding-left: 40px;">2. Search Channels <span style="float: right;">15</span></p> <p style="padding-left: 40px;">3. Lower limit on the Higgs mass, before 2000 <span style="float: right;">16</span></p> <p style="padding-left: 20px;">E. Indications of the Higgs boson at the Tevatron <span style="float: right;">16</span></p> <p style="padding-left: 20px;">F. The LHC and the Discovery of the Higgs <span style="float: right;">17</span></p> <p style="padding-left: 40px;">1. The ATLAS Experiment <span style="float: right;">18</span></p> <p style="padding-left: 40px;">2. Indication of the Higgs boson at the LHC <span style="float: right;">20</span></p> <p style="padding-left: 40px;">3. Production mechanisms <span style="float: right;">20</span></p> <p style="padding-left: 40px;">4. Event Selection <span style="float: right;">21</span></p> <p style="padding-left: 40px;">5. Backgrounds and estimation strategies <span style="float: right;">22</span></p> <p style="padding-left: 20px;">G. Final Data and Observations <span style="float: right;">22</span></p> <p style="padding-left: 20px;">H. Combined Analysis and Higgs Mass Measurement <span style="float: right;">22</span></p> <p style="padding-left: 20px;">I. Conclusive Results <span style="float: right;">22</span></p> <p>IV. Higgs Boson Interaction Map and Measurements <span style="float: right;">22</span></p> <p style="padding-left: 20px;">A. Input Measurements <span style="float: right;">23</span></p> <p style="padding-left: 20px;">B. Signal Strength <span style="float: right;">24</span></p> <p style="padding-left: 20px;">C. Higgs Boson Coupling Strength <span style="float: right;">24</span></p> <p style="padding-left: 40px;">1. Model-I <span style="float: right;">25</span></p> <p style="padding-left: 40px;">2. Model-II <span style="float: right;">25</span></p> <p style="padding-left: 40px;">3. Model-III <span style="float: right;">25</span></p> <p style="padding-left: 20px;">D. Higgs Mass and Lifetime <span style="float: right;">26</span></p> <p style="padding-left: 40px;">1. Theoretical Constraints on the Higgs Mass <span style="float: right;">27</span></p> <p style="padding-left: 40px;">2. Higgs Decay Width and Lifetime <span style="float: right;">27</span></p> <p style="padding-left: 40px;">3. Challenges in Measuring the Width <span style="float: right;">27</span></p> <p style="padding-left: 40px;">4. Challenges and Assumptions <span style="float: right;">28</span></p>
---	--

5. Future Improvements	28
E. Spin	28
1. Theoretical Framework: EFT Approach	28
2. Possible Spin Hypotheses	28
3. Experimental Tests and Results	28
F. Constraining Higgs Spin and CP Properties Using Angular Distributions and Cross-Section Analysis	29
1. Momentum Definitions in the Higgs Rest Frame	29
2. Angular Definitions	29
G. CP Properties	29
1. Symmetry Transformations	29
2. Transforming to Momentum-Spin Space	30
3. Observables and Symmetry Tests	30
4. CP Tests at Hadron Colliders	30
5. Studying Higgs Symmetries (C, P, T) at the LHC	30
6. Higgs-Fermion Interactions (CP Violation)	30
7. Higgs-Gauge Interactions (CP Violation at Dimension-6)	31
V. Latest Developments and Future Outlooks	32
A. ATLAS Run-3 Assets	32
B. Transformer-Based Measurements of $ttH$	32
C. Off-Shell Higgs Production from $ZZ$ Leptonic Decays	33
1. Dependence of $\sigma$ on off-shell $v/s$ on-shell measurements	33
D. Constraints on Higgs Self-Coupling	34
Conclusion	34
Acknowledgements	35
References	35

## INTRODUCTION

The Higgs mechanism is the process by which gauge bosons, such as the  $W$  and  $Z$  bosons in the Standard Model, acquire mass without violating gauge invariance. This mechanism is fundamental to the electroweak theory developed by Weinberg, Salam, and Glashow. The Weinberg–Salam model, independently formulated in the late 1960s, unifies electromagnetic and weak interactions through a gauge theory based on the symmetry group  $SU(2) \times U(1)$ . This unification explains key phenomena such as weak interactions, neutral currents, and spontaneous symmetry breaking, thereby establishing the foundations of modern electroweak theory.

The Higgs boson, sometime called the Higgs particle<sup>1</sup>, plays an important role in our studies of the Standard

Model (SM) and fundamental properties. In this paper, we wish to review various properties of the Higgs. Section I deals with the theoretical grounds of the existence of the Higgs particle, the notion of symmetry breaking and extensions of the SM Higgs. Section II deals with the interactions of the Higgs with other SM particles, which is followed by section III, wherein we see implications of such interactions and how they were utilised to discover the Higgs boson in 2012. Thereafter, in Section IV, we explore experiments that probe characteristic properties of the Higgs, its mass, lifetimes, spin properties and so on. Finally in Section V, we briefly touch upon some current experiments involving the Higgs that display unprecedented precision and technical advancements.

## I. THEORETICAL FRAMEWORK

In quantum field theory, particles arise as excitations of underlying fields, and their mass is not intrinsic but is generated through interactions. In the Standard Model, particles acquire mass via interactions with the Higgs field, a ubiquitous scalar field that permeates all space. Without this mechanism, fundamental particles such as electrons and quarks would remain massless, travel at the speed of light, and be incapable of forming atoms. The weak bosons obtain mass as the Higgs field, upon acquiring a nonzero vacuum expectation value (VEV), spontaneously breaks the  $SU(2)_L \times U(1)_Y$  symmetry. In contrast, the photon and gluon remain massless because the symmetries associated with electromagnetism ( $U(1)_{\text{EM}}$ ) and quantum chromodynamics ( $SU(3)_C$ ) remain unbroken.

Spontaneous symmetry breaking refers to the phenomenon wherein the underlying laws remain symmetric while the realized ground state does not exhibit the full symmetry. In particle physics, the breaking of a continuous global symmetry yields massless Goldstone bosons as predicted by Goldstone’s theorem. However, when such a symmetry is gauged, the would-be Goldstone bosons are absorbed by the gauge fields, which subsequently acquire mass. This absorption—the transformation of Goldstone bosons into the longitudinal polarization components of massive gauge bosons—is the essence of the Higgs mechanism.

### A. Goldstone’s Theorem and Its Limitations in Gauge Theories

Goldstone’s theorem asserts that a continuous global symmetry that is spontaneously broken results in the appearance of massless scalar bosons. In a theory described by a Lagrangian  $\mathcal{L}$  that is invariant under a Lie group  $G$ , if the vacuum expectation value of a field breaks  $G$  to a subgroup  $H$ , the number of massless modes equals the number of broken generators. Mathematically, if a set of scalar fields  $\phi^a$  develops a nonzero VEV, the correspond-

<sup>1</sup> It is also referred to as the God Particle in popular media

ing Noether currents  $J^{\mu a}$  satisfy  $\partial_\mu J^{\mu a} = 0$ . When the symmetry is local, however, these Goldstone modes are not observed as independent particles; instead, they are absorbed by the gauge fields, which become massive. In the limit of a vanishing gauge coupling  $g$ , the gauge fields revert to massless particles, and the Goldstone bosons reappear as physical excitations.

## B. The Higgs Mechanism

The Higgs mechanism provides a self-consistent method for generating mass for gauge bosons while preserving gauge invariance. Consider a complex scalar field  $\phi$  with the Lagrangian

$$\mathcal{L} = \partial_\mu \phi^\dagger \partial^\mu \phi - V(\phi),$$

where the potential

$$V(\phi) = -\mu^2 |\phi|^2 + \lambda |\phi|^4$$

ensures stability ( $\lambda > 0$ ) and induces spontaneous symmetry breaking through the tachyonic mass term  $-\mu^2$ . Minimization of the potential yields a vacuum expectation value  $\langle \phi \rangle = v/\sqrt{2}$  with  $v = \mu/\sqrt{\lambda}$ . In a global  $U(1)$  theory, this symmetry breaking would result in the appearance of a massless Goldstone boson. However, when the symmetry is local, as in the presence of a gauge field  $A_\mu$  with the covariant derivative  $D_\mu = \partial_\mu - igA_\mu$ , the Goldstone boson is absorbed. Parameterizing the field around the VEV as

$$\phi = \frac{1}{\sqrt{2}} (v + h(x)) e^{i\theta(x)/v},$$

one can remove the Goldstone mode  $\theta(x)$  by choosing the unitary gauge. The gauge field then acquires a mass term of the form  $\frac{1}{2}g^2v^2A_\mu A^\mu$ , so that the gauge boson mass is given by  $M_A = gv$ . The inclusion of kinetic terms for both fields and the symmetry-breaking potential ensures that the gauge invariance is maintained while the required mass is generated.

### 1. Higgs Mechanism in Electroweak Theory

In the electroweak theory based on  $SU(2)_L \times U(1)_Y$ , the Higgs field is introduced as a complex  $SU(2)$  doublet,

$$\Phi = \begin{pmatrix} \phi^+ \\ \phi^0 \end{pmatrix},$$

which acquires a nonzero VEV,

$$\langle \Phi \rangle = \frac{1}{\sqrt{2}} \begin{pmatrix} 0 \\ v \end{pmatrix}, \quad v = \frac{\mu}{\sqrt{\lambda}}.$$

This VEV breaks  $SU(2)_L \times U(1)_Y$  down to  $U(1)_{\text{EM}}$ , yielding masses for the weak gauge bosons,

$$M_W = \frac{1}{2}gv, \quad M_Z = \frac{1}{2}\sqrt{g^2 + g'^2}v,$$

while leaving the photon massless ( $M_\gamma = 0$ ). Additionally, the physical Higgs boson, corresponding to the excitation  $h(x)$  around the VEV, has a mass given by

$$M_H = \sqrt{2\lambda}v.$$

For  $v \approx 246$  GeV and  $\lambda \approx 0.13$ , the resulting  $M_H \approx 125$  GeV is in agreement with the experimental observation at the LHC.

## C. Mass Generation and Boson Mixing

When the Higgs mechanism breaks the electroweak symmetry  $SU(2)_L \times U(1)_Y$  down to  $U(1)_{\text{EM}}$ , the gauge bosons acquire mass. The Higgs doublet develops a vacuum expectation value (VEV) given by

$$\langle H \rangle = \frac{1}{\sqrt{2}} \begin{bmatrix} 0 \\ v \end{bmatrix},$$

and its covariant derivative,

$$D_\mu H = \left( \partial_\mu - i\frac{g}{2}W_\mu^a \tau^a - i\frac{g'}{2}B_\mu \right) H, \quad (1)$$

when inserted into the kinetic term  $\mathcal{L} = |D_\mu H|^2$ , leads to mass terms for the gauge bosons. In particular, the charged  $W^\pm$  bosons, defined by

$$W^\pm = \frac{1}{\sqrt{2}}(W^1 \mp iW^2),$$

acquire a mass

$$M_W = \frac{1}{2}gv.$$

The neutral gauge bosons  $W_\mu^3$  and  $B_\mu$  mix[1] to form the physical  $Z$  boson and the photon  $A_\mu$ . This mixing is characterized by the Weinberg angle  $\theta_W$ , with the fields related by

$$Z_\mu = \cos \theta_W W_\mu^3 - \sin \theta_W B_\mu, \quad A_\mu = \sin \theta_W W_\mu^3 + \cos \theta_W B_\mu,$$

and the angle defined via  $\tan \theta_W = \frac{g'}{g}$ . The mass of the  $Z$  boson is then

$$M_Z = \frac{1}{2}\sqrt{g^2 + g'^2}v, \quad (2)$$

while the photon remains massless. These expressions imply the relation

$$M_Z = \frac{M_W}{\cos \theta_W}, \quad (3)$$

a critical prediction of the Standard Model confirmed by experiment.

Neutral current interactions, mediated by the  $Z$  boson, naturally emerge within this framework. The interaction Lagrangian

$$\mathcal{L}_{\text{NC}} = \frac{g}{\cos \theta_W} \bar{f} \gamma^\mu (g_V - g_A \gamma^5) f Z_\mu \quad (4)$$

features vector and axial-vector couplings given by

$$g_V = T^3 - 2Q \sin^2 \theta_W \quad \text{and} \quad g_A = T^3,$$

where  $T^3$  and  $Q$  represent the weak isospin and electric charge of the fermion  $f$ . The existence of neutral current interactions was substantiated by neutrino scattering experiments, thereby lending strong support to the Weinberg–Salam model.

Fermion masses are generated via Yukawa interactions, as expressed by

$$\mathcal{L}_Y = -y_f \bar{\psi}_L \Phi \psi_R + \text{h.c.},$$

such that when  $\Phi$  acquires a VEV, the fermion masses become

$$M_f = \frac{y_f v}{\sqrt{2}}. \quad (5)$$

This mechanism elegantly explains how fermions acquire mass while preserving gauge invariance. A comparison between the abelian and electroweak Higgs mechanisms further illustrates that, while the former, based on a  $U(1)$  gauge theory, involves a complex scalar field with a VEV  $v = \mu/\sqrt{\lambda}$  and a single gauge boson mass  $m_A = ev$ , the electroweak theory utilizes an  $SU(2)_L \times U(1)_Y$  symmetry and a Higgs doublet with  $v \approx 246$  GeV to simultaneously generate the masses of the  $W^\pm$  and  $Z$  bosons, leaving the photon massless.

#### D. Higgs Potential

The Higgs potential, defined as

$$V(\Phi) = -\mu^2 \Phi^\dagger \Phi + \lambda (\Phi^\dagger \Phi)^2,$$

exhibits the characteristic Mexican hat shape, indicating spontaneous symmetry breaking. By expressing the Higgs doublet in terms of real component fields,

$$\Phi = \frac{1}{\sqrt{2}}(\phi_1 + i\phi_2),$$

the potential may be rewritten as

$$V(\phi_1, \phi_2) = -\frac{\mu^2}{2}(\phi_1^2 + \phi_2^2) + \frac{\lambda}{4}(\phi_1^2 + \phi_2^2)^2.$$

For  $\mu^2 < 0$ , the minimum of the potential occurs when

$$\phi_1^2 + \phi_2^2 = \frac{-\mu^2}{\lambda},$$

which results in the nonzero VEV that drives spontaneous symmetry breaking.

The dynamics of small fluctuations around the vacuum are governed by the linearized equations of motion for the scalar and gauge fields.

#### 1. Oscillations in the Higgs Potential

After symmetry breaking, two types of oscillations occur:

- **Radial (Higgs mode):** Fluctuations in the Higgs boson mass, with mass given by  $m_h^2 = 2\lambda v^2$ .
- **Angular (Goldstone mode):** Corresponds to massless modes, which are "eaten" by gauge bosons, making them massive.

Damped oscillations occur due to Higgs boson decay into Standard Model particles, such as  $h \rightarrow 2Z, 2W, b\bar{b}, gg, \gamma\gamma$ . In cosmology, Higgs oscillations could impact early universe dynamics, including reheating after inflation.

#### 2. Equations of Motion for Fluctuations

The system contains small oscillations  $\Delta\phi_1, \Delta\phi_2, A_\mu$  around the vacuum.

The equations of motion for these fluctuations are[2]:

$$\partial_\mu \{ \partial^\mu (\Delta\phi_1) - e\phi_0 A^\mu \} = 0, \quad (6)$$

$$(\partial^2 - 4\phi_0^2 V''(\phi_0^2)) \Delta\phi_2 = 0, \quad (7)$$

$$\partial^\nu F_{\mu\nu} = e\phi_0 \{ \partial_\mu (\Delta\phi_1) - e\phi_0 A_\mu \}. \quad (8)$$

The derived equations indicate:

- One massive scalar field ( $\Delta\phi_2$ ) with  $m_{\phi_2}^2 = (2\phi_0)^2 V''(\phi_0^2)$ .
- The Goldstone boson disappears, giving mass to  $A_\mu$  via the Higgs mechanism.
- The gauge boson acquires mass  $m_A = e\phi_0$ .
- If  $e = 0$ , both the gauge and Goldstone bosons remain massless.
- Mass generation is directly tied to gauge interactions.

By redefining the gauge field as

$$B_\mu = A_\mu - \frac{1}{e\phi_0} \partial_\mu (\Delta\phi_1),$$

and noting that the corresponding field strength tensor  $G_{\mu\nu}$  equals  $F_{\mu\nu}$ , the equations simplify to the Lorenz condition  $\partial_\mu B^\mu = 0$  and the Proca equation

$$\partial^\nu G_{\mu\nu} + e^2 \phi_0^2 B_\mu = 0,$$

explicitly demonstrating that the vector boson acquires a mass  $m_A = e\phi_0$ .

## E. Spontaneous Symmetry Breaking in Non-Abelian Theories

When symmetry breaking occurs in a semisimple gauge group, different irreducible representations for scalars lead to various mass generation mechanisms. Gauge fields always belong to the adjoint representation of the symmetry group.

### 1. *SU(3) Example: Scalars in the Octet Representation*

Consider a scalar octet under SU(3). Two components of the scalar field acquire vacuum expectation values (VEVs) corresponding to states with  $Y = 0$  and  $I_3 = 0$ . These two components do not get absorbed into gauge bosons. The remaining six components of the scalar octet do not develop VEVs but instead mix with the corresponding gauge bosons via the Higgs mechanism and get absorbed. As a result, six gauge bosons acquire mass.

### 2. *Structure of Vector Boson Masses*

The mass spectrum consists of:

- Two  $I = 1/2$  vector doublets (with mass degeneracy broken by electromagnetic interaction, which leads to mass splitting),
- An  $I = 1$  triplet, whose masses arise purely from electromagnetic interactions.

This suggests that these would be massless in the absence of electromagnetic effects.

### 3. *Residual Unbroken Symmetry*

Two massless gauge bosons remain, corresponding to the unbroken Abelian group generated by  $Y$  and  $I_3$ . This suggests that an Abelian subgroup of SU(3) remains intact. The massless gauge bosons would correspond to a photon-like field and another massless neutral boson.

### 4. *Implications for Electroweak Symmetry Breaking*

A further mechanism (e.g., weak interactions) breaks hypercharge conservation, giving mass to one of the remaining gauge bosons. The photon remains massless after all symmetry breaking steps, as in the Standard Model.

### 5. *Incomplete Multiplets*

After symmetry breaking, some gauge bosons and scalars become massive while others remain massless.

This leads to incomplete multiplets, deviating from the original full symmetry representation. This means that the symmetry-breaking pattern does not preserve the complete multiplet structure.

## F. Generalization to Composite Higgs Models

If symmetry-breaking scalar fields are not fundamental but arise from bilinear combinations of fermions (e.g.,  $\Phi \sim \bar{\psi}\psi$ ), the same symmetry-breaking patterns still occur. This suggests a possible dynamical origin for mass generation in strongly coupled gauge theories, such as Technicolor models.

## G. Experimental Confirmation and Open Questions

- The Higgs boson was discovered at ATLAS and CMS at CERN in 2012 with  $M_H \approx 125$  GeV.

The electroweak theory was validated in several key experiments:

- **Neutral current discovery (1973):** Confirmed the existence of  $Z$ -mediated weak interactions.
- **$W$  and  $Z$  boson discovery (1983):** At CERN, provided direct evidence for electroweak unification.
- **Higgs boson discovery (2012):** At the LHC, confirmed the Higgs mechanism, solidifying the Standard Model's predictions.

Open questions remain:

- **Hierarchy Problem:** Why is  $M_H \ll M_{\text{Planck}}$ ?
- **Higgs and Dark Matter:** Could Higgs interactions explain dark matter?

## H. Mass Constraint on the Higgs Boson

The spontaneous symmetry breaking (SSB) sector of the Standard Model (SM) has long been uncertain.

### 1. *Higgs Sector Possibilities*

- **Simplest case:** An elementary Higgs doublet acquires a vacuum expectation value (VEV).
- **More complex cases:** Multiple Higgs doublets (e.g., in supersymmetric models) or different Higgs representations.
- **Dynamical symmetry breaking:** Possible without elementary scalars (e.g., Technicolor).

- The 2012 discovery of a Higgs-like boson at 125 GeV supports the elementary Higgs model.
- However, early Higgs coupling measurements were not precise enough to rule out alternatives.

## 2. Higgs Mass Constraints

In the SM, only one physical Higgs boson remains after SSB. The Higgs mass is given by:

$$M_H = \sqrt{2\lambda v^2} \quad (9)$$

where  $\lambda$  is the quartic self-coupling and  $v = 246$  GeV is the vacuum expectation value:

$$v = \sqrt{2}\langle 0|\phi^0|0\rangle \quad (10)$$

Couplings to particles are proportional to their masses:

$$\frac{M}{v}, \quad \frac{M^2}{v}, \quad \text{or} \quad \left(\frac{M}{v}\right)^2 \quad (11)$$

These couplings are small except for the top quark, making the Higgs difficult to produce or detect. Gauge boson couplings (to  $W$  and  $Z$ ) are proportional to their masses:

$$g^2 v \sim \frac{M^2}{v} \quad (12)$$

making them more promising channels for Higgs detection.

## 3. Theoretical Constraints

The Higgs mass and quartic coupling are related as:

$$M_H^2 = 2\lambda v^2 \quad (13)$$

$$\lambda = \frac{g^2 M_H^2}{8M_W^2} = \frac{G_F M_H^2}{\sqrt{2}} \quad (14)$$

with

$$v \approx 246 \text{ GeV}, \quad G_F \approx 1.2 \times 10^{-5} \text{ GeV}^{-2} \quad (15)$$

The only basic constraint on  $\lambda$  at tree-level is vacuum stability:

$$\lambda > 0 \quad (16)$$

which allows  $M_H$  values ranging from 0 to infinity.

## 4. Renormalization Group Constraints

The running gauge couplings follow renormalization group equations. One-loop coefficients for the Standard Model gauge groups  $SU(3), SU(2), U(1)$  are given by:

$$b_{g_s} = \frac{1}{16\pi^2} \left( 11 - \frac{4F}{3} \right) \rightarrow -\frac{1}{16\pi^2} (7) \quad (17)$$

$$b_g = \frac{1}{16\pi^2} \left( \frac{22}{3} - \frac{4F}{3} - \frac{n_H}{6} \right) \rightarrow -\frac{1}{16\pi^2} \left( \frac{19}{6} \right) \quad (18)$$

$$b_{g'} = \frac{1}{16\pi^2} \left( \frac{20F}{9} + \frac{n_H}{6} \right) \rightarrow +\frac{1}{16\pi^2} \left( \frac{41}{6} \right) \quad (19)$$

These expressions are valid at energy scales  $Q^2 \gg m_t^2, v^2$ .

## 5. Running of Yukawa Couplings

The one-loop running equations for the Higgs quartic coupling  $\lambda(Q^2)$  and the top Yukawa coupling  $h_t$  are:

$$\frac{d\lambda(Q^2)}{d\ln Q^2} = \frac{1}{32\pi^2} \left( 24\lambda^2 + 24h_t^2\lambda - 4h_t^4 - 3\lambda(3g^2 + g'^2) + \frac{3}{8} [2g^4 + (g^2 + g'^2)^2] \right) \quad (20)$$

$$\frac{dh_t(Q^2)}{d\ln Q^2} = \frac{1}{32\pi^2} \left( 9h_t^3 - h_t \left( 8g_s^2 + \frac{9}{4}g^2 + \frac{17}{12}g'^2 \right) \right) \quad (21)$$

The couplings on the right-hand side are understood to be running couplings evaluated at the scale  $Q^2$ .

## 6. Triviality Bound on $M_H$

Typically one loop diagrams contribute to the running of  $\lambda$

The upper bound on the Higgs mass is due to the triv-

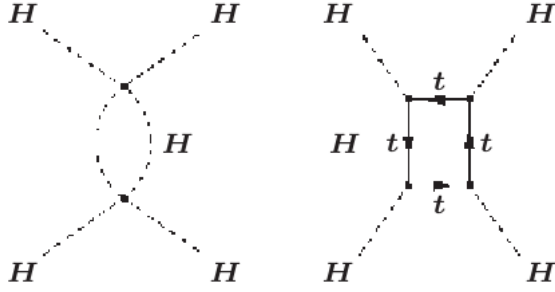


FIG. 1: Diagrams contributing to Higgs self-coupling and Yukawa coupling running at one-loop??.

iality constraint From equation (30) : For  $M_H \gtrsim 350$  GeV,  $\lambda(\mu^2)$  becomes larger than unity. For  $M_H \sim 173$  GeV,  $h_t \sim 0.7$

For large  $M_H$ , the first term on the RHS dominates, and solving the equation gives:

$$\lambda(Q^2) = \frac{\lambda(\mu^2)}{1 - \frac{3\lambda(\mu^2)}{4\pi^2} \ln(Q^2/v^2)}$$

The quartic coupling  $\lambda(Q^2)$  diverges at the Landau pole  $Q_{LP}$ , given by:

$$Q_{LP} = v e^{\frac{2\pi^2}{3\lambda(\mu^2)}} \quad (22)$$

This divergence suggests that the theory loses validity if  $Q_{LP}$  is within the physical domain.

To maintain a consistent weakly coupled theory,  $Q_{LP}$  must be above the scale where new physics appears.

This leads to the triviality bound on the Higgs mass:

$$M_H < \sqrt{\frac{2\sqrt{2}\pi^2}{3G_F \ln(\Lambda/v)}} \quad (23)$$

where  $\Lambda$  is the new physics scale, and the Planck scale is  $M_P \sim 1.2 \times 10^{19}$  GeV.

Approximate values:

- If  $\Lambda \sim M_P$ , then  $M_H \lesssim O(140)$  GeV.
- If  $\Lambda \sim 1500$  GeV, then  $M_H \lesssim O(650)$  GeV.

The upper bound on  $M_H$  is somewhat uncertain because the one-loop approximation becomes invalid for large  $M_H$ , leading to the breakdown of perturbation theory. However, it still provides an estimate of the maximum Higgs mass consistent with a weakly coupled field theory (see Figure 2). Notably, if a Higgs boson heavier than 200 GeV had been observed, it would have strongly indicated the presence of new physics at a relatively low energy scale.

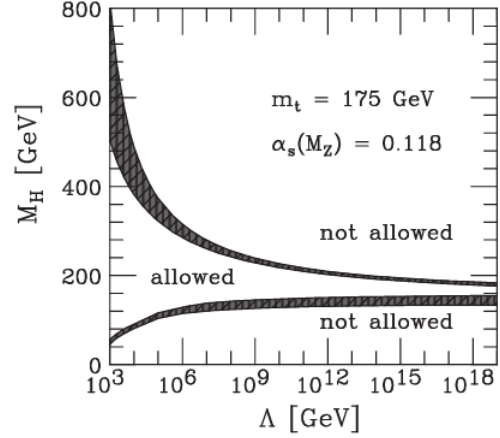


FIG. 2: Theoretical constraints on Higgs mass from triviality and stability arguments

A more detailed evaluation, including two-loop effects and previously neglected terms, refines the Higgs mass bounds.

- If  $\Lambda \sim M_P$ , then  $M_H \sim 180$  GeV.
- If  $\Lambda \sim 2M_P$ , then  $M_H \sim 700$  GeV.

Non-perturbative lattice calculations suggest an absolute upper bound of 650–700 GeV

Vacuum Stability and the Lower Bound on  $M_H$

The Higgs mass also has a lower limit from vacuum stability

For small  $\lambda$ , the first equation (34) and (35) simplifies, keeping only the dominant  $h_t^4$  term:

$$\lambda(Q^2) \approx \lambda(v^2) - \frac{3h_t^4}{4\pi^2} \ln \frac{Q^2}{v^2} \quad (24)$$

If  $\lambda(Q^2)$  turns negative, the vacuum becomes unstable.

This condition sets a lower bound on the Higgs mass for  $Q = \Lambda$  :

$$M_H^2 = \frac{3h_t^4 v^2}{2\pi^2 G_F} \ln \frac{Q}{v} \quad (25)$$

and

$$\lambda(v^2) = \frac{3h_t^4}{4\pi^2} \ln \frac{Q^2}{v^2} \quad (26)$$

Therefore, For  $\Lambda = 1500$  GeV,  $M_H \approx 85$  GeV. For large  $\Lambda$ , it is necessary to account for the running of  $h_t$ , two-loop effects, and additional loop contributions to the effective potential.

Typical results indicate that for  $\Lambda = M_P$ ,  $M_H$  lies in the range 130–180 GeV, with a slightly broader range for smaller  $\Lambda$ .

If a long-lived metastable vacuum is considered, the lower bound can drop to around 115 GeV

However, these constraints do not apply to the Minimal Supersymmetric Standard Model (MSSM), where  $\lambda$  is not independent and additional RGE contributions exist.

In the MSSM, the lightest Higgs mass is limited to 135 GeV (or 150 GeV in singlet extensions).

A Higgs significantly heavier or lighter than 135 GeV could have distinguished between the SM and supersymmetry, but the observed 125 GeV remains inconclusive and presents challenges for both frameworks.

### I. The Problem Without the Higgs Mechanism

In a gauge theory such as Quantum Electrodynamics (QED) or electroweak theory, the requirement of gauge invariance and renormalizability forces the gauge bosons to be massless. If one attempts to add a naive mass term for a gauge boson,

$$\mathcal{L}_{\text{mass}} = \frac{1}{2} m_A^2 A^\mu A_\mu, \quad (27)$$

gauge invariance is explicitly broken because under a gauge transformation the field  $A_\mu$  shifts, and the resulting loss of symmetry undermines the cancellations that ensure renormalizability. In the absence of the Higgs mechanism, the longitudinal polarization states of massive gauge bosons produce scattering amplitudes that grow with energy (e.g. in processes such as  $W^+W^- \rightarrow W^+W^-$  where the amplitude increases as  $E^2$ ), thus violating unitarity at high energies. Moreover, introducing explicit fermion mass terms would break chiral gauge symmetry and lead to additional non-renormalizable interactions. Without the Higgs mechanism, these combined issues—violation of gauge invariance, loss of renormalizability, problematic high-energy behavior, and the inability to generate fermion masses consistently—render a massive gauge theory theoretically unsound.

The Higgs mechanism restores consistency by providing a gauge-invariant and renormalizable method to generate masses. Spontaneous symmetry breaking allows the Goldstone bosons, which would otherwise arise from the breaking of continuous symmetries, to be absorbed by the gauge fields, thus endowing them with a longitudinal degree of freedom and a physical mass. In this framework, the gauge-invariant Lagrangian remains intact, and the observed massive  $W^\pm$  and  $Z$  bosons, together with the massless photon, are naturally explained. Consequently, the Standard Model is able to accommodate the observed particle masses without sacrificing its theoretical consistency.

### J. Naturalness and the Higgs Boson in the Standard Model

The concept of "naturelessness" (or lack of naturalness) in physics refers to situations where fundamental

parameters require extreme fine-tuning to match. This issue is particularly prominent in the case of the Higgs boson, whose mass appears unnaturally small given the quantum corrections it receives. This discrepancy is known as the **hierarchy problem** and suggests the need for new physics beyond the Standard Model (SM). **Hierarchy Problem:** Without new physics, the Higgs boson mass is highly sensitive to high-energy scales, leading to severe fine-tuning issues to keep the Higgs mass near the electroweak scale. The Higgs potential is given by

$$V(\Phi) = -\mu^2 \Phi^\dagger \Phi + \lambda (\Phi^\dagger \Phi)^2, \quad (28)$$

where the doublet field  $\Phi$  acquires a vacuum expectation value (VEV)

$$v = \sqrt{\frac{\mu^2}{\lambda}} \approx 246 \text{ GeV}. \quad (29)$$

After symmetry breaking, the physical Higgs boson mass is

$$m_H = \sqrt{2\lambda} v \approx 125 \text{ GeV}. \quad (30)$$

#### 1. Fermion Loop Corrections (Top Quark Contribution)

However, the Higgs mass is highly sensitive to quantum corrections. Loop contributions from heavy particles, notably the top quark, introduce quadratic divergences. For instance, the leading top quark loop correction is approximately

$$\Delta m_H^2 \sim \frac{3|y_t|^2}{8\pi^2} \Lambda^2, \quad (31)$$

where:

- $y_t$  is the top Yukawa coupling ( $\approx 1$ ),
- $\Lambda$  is the energy scale cutoff.

For  $\Lambda \sim M_{\text{Planck}} \approx 10^{19} \text{ GeV}$ , the correction is enormous:

$$\Delta m_H^2 \sim 10^{34} \text{ GeV}^2 \quad (32)$$

which requires extreme fine-tuning to obtain  $m_H^2 \sim (125 \text{ GeV})^2$ .

#### 2. Gauge Boson Loop Corrections

W and Z bosons contribute corrections:

$$\Delta m_H^2 \sim \frac{g^2}{16\pi^2} \Lambda^2 \quad (33)$$

where  $g$  is the electroweak coupling constant.



### 3. Higgs Self-Interaction Corrections

The Higgs boson itself contributes to its mass via:

$$\Delta m_H^2 \sim \frac{\lambda}{16\pi^2} \Lambda^2 \quad (34)$$

which also leads to large corrections.

Since all these corrections grow with  $\Lambda^2$ , the Higgs mass must be fine-tuned to cancel these large contributions—a hallmark of naturelessness. This extreme sensitivity, known as the hierarchy problem, points to the unnatural fine-tuning within the Standard Model.

The apparent unnaturalness of the Higgs mass has inspired several proposals to address the hierarchy problem. Supersymmetry (SUSY) is one compelling solution in which every Standard Model particle is paired with a superpartner; the contributions from these superpartners cancel the quadratic divergences arising from the Standard Model loops. In composite Higgs models, the Higgs is not fundamental but emerges as a bound state of a new strongly interacting sector, thereby softening the sensitivity to high-energy scales. Alternative ideas, including models with extra dimensions or even anthropic considerations within a multiverse framework, have also been proposed. Each approach seeks to explain why the Higgs mass remains close to the electroweak scale without fine-tuning, thus preserving naturalness.

Taken together, these issues highlight that while the Standard Model successfully describes the mass generation of gauge bosons via the Higgs mechanism, the hierarchy problem and related naturalness concerns suggest that new physics may be required to fully understand the electroweak scale. Continued theoretical and experimental investigations, including precision measurements at colliders and searches for supersymmetry or other new phenomena, remain essential to resolve these fundamental questions.

### K. Feynman Rules

In this section we summarize the key Feynman rules relevant to the Higgs sector. The free propagator of the Higgs boson is given by

$$\frac{i}{p^2 - m_h^2 + i\epsilon}, \quad (35)$$

where  $p$  is the four-momentum,  $m_h$  is the Higgs mass, and the term  $i\epsilon$  enforces the correct contour prescription.

The Standard Model Yukawa Lagrangian,

$$\mathcal{L}_Y = - \sum_f \left( \frac{m_f}{v} \right) h \bar{f} f, \quad (36)$$

describes the coupling of the Higgs boson to fermions, where  $v \approx 246$  GeV is the Higgs vacuum expectation value and  $m_f$  is the fermion mass. The corresponding Feynman rule for a vertex with a Higgs and

a fermion–antifermion pair is

$$-i \frac{m_f}{v}. \quad (37)$$

Interactions with the electroweak gauge bosons arise from the kinetic term of the Higgs doublet. For the  $W$  bosons, the interaction term

$$\mathcal{L}_{hWW} = \frac{m_W^2}{v} h W^{+\mu} W_{\mu}^{-} \quad (38)$$

leads to the Feynman rule for a vertex with one Higgs and two  $W$  bosons,

$$i g m_W g_{\mu\nu}, \quad (39)$$

where  $g = \frac{e}{\sin \theta_W}$ . Similarly, the interaction term for the  $Z$  boson is

$$\mathcal{L}_{hZZ} = \frac{m_Z^2}{2v} h Z^{\mu} Z_{\mu}, \quad (40)$$

with the vertex given by

$$i \frac{g m_Z}{\cos \theta_W} g_{\mu\nu}. \quad (41)$$

Direct Higgs couplings to photons and gluons do not occur at tree level. Instead, effective interactions are generated at one-loop. The effective Lagrangian for Higgs coupling to photons is

$$\mathcal{L}_{h\gamma\gamma} = -\frac{\alpha}{8\pi v} h F^{\mu\nu} F_{\mu\nu} \sum_i Q_i^2 A_i, \quad (42)$$

leading to an effective vertex of

$$\frac{i\alpha}{\pi v} F^{\mu\nu} F_{\mu\nu}. \quad (43)$$

Likewise, the effective interaction for Higgs coupling to gluons is expressed as

$$\mathcal{L}_{hgg} = -\frac{\alpha_s}{12\pi v} h G^{a\mu\nu} G_{\mu\nu}^a, \quad (44)$$

with the effective vertex

$$\frac{i\alpha_s}{\pi v} G^{a\mu\nu} G_{\mu\nu}^a. \quad (45)$$

The self-interactions of the Higgs boson stem from its potential,

$$V(h) = \frac{m_h^2}{2} h^2 + \lambda v h^3 + \frac{\lambda}{4} h^4, \quad (46)$$

where  $\lambda = \frac{m_h^2}{2v^2}$ . This potential yields the trilinear vertex (three-Higgs interaction) with the Feynman rule

$$-i \frac{3m_h^2}{v}, \quad (47)$$

and the quartic vertex (four-Higgs interaction) with

$$-i \frac{3m_h^2}{v^2}. \quad (48)$$

Interaction	Lagrangian Term	Feynman Rule
Higgs propagator	$\frac{i}{p^2 - m_h^2 + i\epsilon}$	—
Higgs-fermion ( $h f \bar{f}$ )	$-\frac{m_f}{v} h \bar{f} f$	$-i \frac{m_f}{v}$
Higgs-W boson ( $h W W$ )	$\frac{m_W^2}{v} h W^{+\mu} W_{\mu}^{-}$	$i g m_W g_{\mu\nu}$
Higgs-Z boson ( $h Z Z$ )	$\frac{m_Z^2}{2v} h Z^{\mu} Z_{\mu}$	$i \frac{g m_Z}{\cos \theta_W} g_{\mu\nu}$
Higgs-photon ( $h \gamma \gamma$ )	Loop-induced	$i \frac{\alpha}{\pi v} F^{\mu\nu} F_{\mu\nu}$
Higgs-gluon ( $h g g$ )	Loop-induced	$i \frac{\alpha_s}{\pi v} G^{a\mu\nu} G_{\mu\nu}^a$
Higgs trilinear ( $h h h$ )	$-\lambda v h^3$	$-i \frac{3m_h^2}{v}$
Higgs quartic ( $h h h h$ )	$-\frac{\lambda}{4} h^4$	$-i \frac{3m_h^2}{v^2}$

TABLE I: Summary of Higgs interactions, displaying the relevant Lagrangian terms and Feynman rules.

## II. HIGGS DECAYS AND INTERACTIONS

The Higgs Boson is a fundamental particle that interacts more strongly with heavier particles. Its decay patterns help scientists test the Standard Model (SM). If the Higgs decays differently than predicted, it could hint at new physics.

### A. Decay to Fermions:

The decay rate depends on the fermion's mass and includes quantum corrections (QCD and electroweak effects). QCD corrections (strong force effects) are significant and are calculated using a “running mass” for quarks. Where mass refers to its mass as it changes with energy scale due to the QCD effects. These variations occur because the strong force interactions modify the quarks' effective mass depending on the energy level at which it is measured.

The Higgs couples more strongly to heavier particles. The leading order decay width for  $h \rightarrow f \bar{f}$ :

$$\Gamma(h \rightarrow f \bar{f}) = \frac{G_F m_f^2 N_c}{4\sqrt{2}\pi} M_h \beta_f^3 \quad (49)$$

Where,  $G_F$  is the Fermi constant (strength of weak force),  $m_f$  is the mass of the fermion,  $N_c$  is the color factor (3 for quarks, 1 for leptons),  $M_h$  is the Higgs mass, and  $\beta_f$  is the velocity factor, near 1 for light fermions.

### B. Including QCD (strong force) effects:

Including QCD corrections is important, especially for  $h \rightarrow b \bar{b}$ . A significant portion of the QCD corrections can be accounted for by expressing the decay width in terms of a running mass,  $m_f(\mu)$  evaluated at the scale  $\mu = M_h$ , indicating that the large effects are triggered by

large logarithms. The QCD corrected decay width can be approximated as,

$$\Gamma(h \rightarrow b \bar{b}) = \frac{3G_F m_b^2 M_h^2}{4\sqrt{2}\pi} \beta_b^3 \left( 1 + 5.67 \frac{\alpha_s(M_h^2)}{\pi} + \dots \right) \quad (50)$$

Where  $\alpha_s(M_h^2)$  is the strong coupling constant defined in the MS-bar scheme with 5 flavors.

### C. Why mostly $h \rightarrow b \bar{b}$ decay?

The Higgs interacts more strongly with heavier particles. The coupling strength is  $y_f = \frac{m_f}{v}$ , where  $v$  is the Higgs vacuum expectation value. The bottom quark is the heaviest quark that the Higgs decays into. Higgs doesn't decay into the top quark because  $m_t = 173$  GeV which is larger than  $M_h/2 = 62.5$  GeV, so the Higgs isn't heavy enough to produce two top quarks.

### D. Higgs decay to weak Bosons (W,Z):

The Higgs is heavy enough to decay to  $W^+ W^-$  or  $ZZ$ . However, if  $M_h < 2M_W$  or  $2M_Z$ , one of the bosons is off-shell (i.e., virtual). Over most of the phase space, we can assume that one of the two gauge bosons decays on its mass shell, while the other is pushed into its sizable Breit-Wigner tails. The decay width for such a decay,  $h \rightarrow ZZ^* \rightarrow f_1(p_1) f_2(p_2) Z(p_3)$  is:

$$\Gamma(h \rightarrow ZZ^*) = \int_{(M_h - M_Z)^2}^{M_h^2} dm_{12}^2 \int_{m_{23}^2}^{m_{23}^2} dm_{23}^2 \frac{|A|^2}{256\pi^3 M_h^3} \quad (51)$$

where  $m_{ij} = (p_i + p_j)^2$ , and  $m_{12}^2 + m_{23}^2 + m_{31}^2 = M_h^2 + M_Z^2$ .

The usual Källén function is  $\lambda = m_1^4 - 2m_1^2(M_h^2 + M_Z^2) + (M_h^2 - M_Z^2)^2$ , and the integration boundaries for  $m_{23}^2$  are given by  $(M_h^2 + M_Z^2 - m_{12}^2 \pm \sqrt{\lambda})/2$ . The amplitude is:

The amplitude squared for the decay  $h \rightarrow Z f \bar{f}$  is given by:

$$|A(h \rightarrow Z f \bar{f})|^2 = 32(g_L^2 + g_R^2)G_F^2 M_Z^4 \left| \frac{2M_Z^2 m_{12}^2 - m_{13}^2 m_{12}^2 - M_h^2 M_Z^2}{(m_{12}^2 - M_Z^2)^2 + \Gamma_Z^2 M_Z^2} + \frac{m_{13}^2 M_Z^2 + m_{13}^2 M_h^2 - m_{13}^4}{(m_{12}^2 - M_Z^2)^2 + \Gamma_Z^2 M_Z^2} \right| \quad (52)$$

where  $g_L = T_f^3 - Q_f s_W^2$ ,  $g_R = -Q_f s_W^2$ , and  $T_f^3 = \pm \frac{1}{2}$ .

Integrating over  $dm_{23}^2$ , we find the differential decay rate:

$$\frac{d\Gamma}{dm_{12}^2}(h \rightarrow Z f \bar{f}) = \frac{(g_L^2 + g_R^2)G_F^2 \sqrt{\lambda} M_Z^4}{48\pi^3 M_h^3} \frac{12M_Z^2 m_{12}^2 + \lambda}{(m_{12}^2 - M_Z^2)^2 + \Gamma_Z^2 M_Z^2} \quad (53)$$

For the decay  $h \rightarrow W f f'$ , the results can be obtained by making the appropriate redefinitions of the fermion-gauge boson couplings. The total decay width for  $h \rightarrow W W^*$  is:

$$\Gamma(h \rightarrow W W^*) = \frac{3g^4 M_h}{512\pi^3} F\left(\frac{M_W}{M_h}\right) \quad (54)$$

For the decay  $h \rightarrow Z Z^*$ , we have:

$$\Gamma(h \rightarrow Z Z^*) = \frac{g^4 M_h}{2048c_W^4 \pi^3} \left(7 - \frac{40}{3}s_W^2 + \frac{160}{9}s_W^4\right) F\left(\frac{M_Z}{M_h}\right) \quad (55)$$

where

$$\begin{aligned} F(x) = & -|1 - x^2| \left[ \frac{47}{2}x^2 - \frac{13}{2} + \frac{1}{x^2} \right] \\ & + 3(1 - 6x^2 + 4x^4) |\log x| \\ & + 3(1 - 8x^2 + 20x^4) \sqrt{4x^2 - 1} \cos^{-1} \left( \frac{3x^2 - 1}{2x^3} \right) \end{aligned}$$

Going beyond the total decay rate and instead studying the  $m_{12}$ -distribution is a powerful tool in studying the Lorentz structure of the  $VVh$  coupling.

### E. Gluons:

The decay of the Higgs Boson into two gluons is a loop-induced process in the Standard Model (SM), meaning, it does not occur at tree level but proceeds through virtual quark loops (primarily top quarks). This process is closely related to Higgs production via gluon fusion ( $gg \rightarrow h$ ). Since both involve the same effective Higgs-gluon coupling. The decay width for  $h \rightarrow gg$  is:

$$\Gamma(h \rightarrow gg) = \frac{G_F \alpha_s^2 M_h^3}{64\sqrt{2}\pi^3} \sum_q F_{1/2}(\tau_q)^2 \quad (56)$$

where  $G_F$  is the Fermi constant,  $\alpha_s$  is the strong coupling constant,  $\tau_q = \frac{4m_q^2}{M_h^2}$ , and  $F_{1/2}(\tau_q)$  is the loop function for spin  $\frac{1}{2}$ .

The loop function encodes the quantum corrections from virtual quarks and is defined as:

$$F_{1/2}(\tau_q) \equiv -2\tau_q [1 + (1 - \tau_q)f(\tau_q)] \quad (57)$$

It includes one power of the Yukawa coupling, expressed in terms of the mass, and the rescaled scalar one-loop three-point function:

$$f(\tau_q) = \begin{cases} \sin^{-1} \left( \sqrt{\frac{1}{\tau_q}} \right)^2 & \text{for } \tau_q \geq 1 \\ -\frac{1}{4} \left[ \log \left( \frac{1 + \sqrt{1 - \tau_q}}{1 - \sqrt{1 - \tau_q}} \right) - i\pi \right]^2 & \text{for } \tau_q < 1 \end{cases} \quad (58)$$

### F. Dominant Contribution:

Top quark ( $t$ ): Since  $m_t \gg M_h/2$ , the top quark dominates the loop contribution. In the limit  $\tau_t \rightarrow \infty$  (very heavy top), the loop function approaches  $F_{1/2}(\tau_t) \rightarrow -4/3$ . This shows non-decoupling behavior even if the top quark still contributes significantly because its Yukawa coupling compensates for its large mass.

For the light quarks such as bottom ( $b$ ),  $M_q \ll M_h$ . The loop function is:

$$F_{1/2}(\tau_b) \rightarrow \frac{2m_b^2}{M_h^2} \log^2 \left( \frac{4m_b^2}{M_h^2} \right) \quad (59)$$

This contribution is suppressed due to the small mass.

Another theoretical aspect we can read is that the top contribution to the effective Higgs-gluon coupling does not vanish for large top masses. The reason for this non-decoupling behavior is that the Yukawa coupling in the numerator exactly cancels the linear kinetic decoupling of fermions from the loop function  $f(\tau_t)$ . We can turn this feature around and use it to probe the existence of heavy quarks which get their mass through a Yukawa coupling to the Higgs field.

### G. Photons:

The decay  $h \rightarrow \gamma\gamma$  is a loop-induced process since the Higgs Boson doesn't couple directly to photons at tree level. The dominant contribution comes from:

1. Fermion loops (especially the top quark due to its large Yukawa coupling)
2.  $W$ -Boson loops (electroweak gauge bosons)
3. Possible Beyond Standard Model (BSM) scalar contribution

The decay width is:

$$\begin{aligned} \Gamma(h \rightarrow \gamma\gamma) = & \frac{\alpha^2 G_F}{128\pi^3} M_H^3 \left| \sum_f N_{c,f} Q_f^2 F_{1/2}^{(f)} + F_1(\tau(W)) + \right. \\ & \left. \sum_S N_{c,S} \frac{g_{hSS}}{m_S^2} F_0(\tau(S)) \right|^2 \end{aligned} \quad (60)$$

Where  $\alpha$  is the fine structure constant,  $Q_f$  is the electric charge of fermions,  $\tau_i = \frac{4m_i^2}{M_h^2}$  (for  $i = f, W, S$ ), and  $F_{1/2}, F_1, F_0$  are the loop functions for fermions,  $W$ -bosons, and scalars respectively.

The scalar loop function  $F_{1/2}(\tau_q)$  is given in Eq. (9), and

$$F_1(\tau_W) = 2 + 3\tau_W [1 + (2 - \tau_W)f(\tau_W)],$$

$$F_0(\tau_S) = \tau_S [1 - \tau_S f(\tau_S)].$$

### H. Loop Functions:

- Fermion loop function  $F_{1/2}$ : It is given by the same expression as in the gluon fusion case (Eqn 9). In the heavy mass limit ( $\tau_f \rightarrow \infty$ ),  $F_{1/2} = 4/3$ .
- $W$ -Boson loop function  $F_1$ : First equation of the above. In the heavy mass limit ( $\tau_W \rightarrow \infty$ ),  $F_1 = 7$ .
- Scalar loop function  $F_0$  (for BSM scalars): Second equation of the above. In the heavy mass limit ( $\tau_s \rightarrow \infty$ ),  $F_0 = -1/3$ .

The top quark and  $W$ -boson contributions interfere destructively due to their opposite signs. The sign of the top Yukawa coupling affects the interference, making decay sensitive to possible BSM modifications.

XX	BR(h $\rightarrow$ XX)	$\delta_{QCD}$	$\delta_{ew}$
bb	0.5824	0.2%	0.5%
gg	$8.187 \times 10^{-2}$	3%	1%
$l^+l^- (l^+l^-)$	$2.745 \times 10^{-4}$	0.5%	
$\tau^+\tau^-$	0.06272	0.5%	
$\gamma\gamma$	$2.27 \times 10^{-3}$	<1%	<1%
$l^+l^- (\nu\bar{\nu})$	$2.338 \times 10^{-8}$		
$\mu^+\mu^-$	$2.176 \times 10^{-4}$	0.5%	
WW	0.215	<0.5%	0.5%
$\nu\bar{\nu} (\nu\bar{\nu})$	$1.044 \times 10^{-3}$		
cc	$2.891 \times 10^{-2}$	0.2%	0.5%
ZZ	$2.619 \times 10^{-2}$	<0.5%	<0.5%
$l^+l^- (q\bar{q})$	$3.668 \times 10^{-3}$		
$Z\gamma$	$1.533 \times 10^{-3}$	5%	<1%
$q\bar{q} (q\bar{q})$	$1.089 \times 10^{-1}$		

TABLE II: For  $M_h = 125$  GeV. In the right column, we show the final states from the  $WW$  and  $ZZ$  decays. For leptons, we sum over  $l = e, \mu, \tau$ , while for quarks, we sum over  $q = u, d, c, s, b$ . The  $\delta$  values are relative theoretical uncertainties due to missing higher orders.[3]

The Higgs branching ratios are shown in Figure 3 for a SM Higgs boson of arbitrary mass.

The width of the curves is an estimate of the theoretical uncertainties on the branching ratios. The branching ratios assume SM couplings and no new decay channels and include all known radiative corrections. Also shown in Fig. 1 is the Higgs total decay width as a function

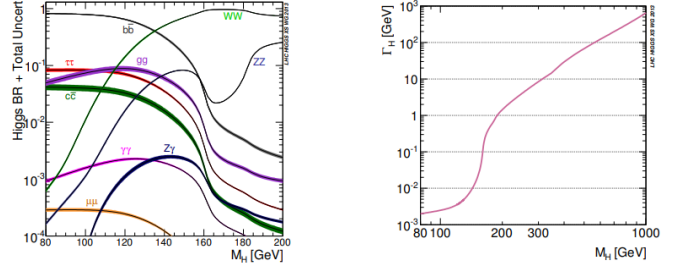


FIG. 3: Left: SM Higgs branching ratios. The widths of the curves are estimates of the theoretical uncertainty.

Right: total width for a SM-like Higgs boson of arbitrary mass. In this figure, H is the SM Higgs boson that is denoted by h in this review

of Higgs mass. For  $M_h = 125$  GeV, the total width is very small,  $\Gamma_h = 4$  MeV  $\ll M_h$ . The reason is that the leading coupling entering the decays is the small bottom Yukawa coupling  $Y_b = \frac{\sqrt{2}m_b}{v}$ . Detailed predictions for the Standard Model branching ratios are given in Table II. Future high precision measurements at the LHC and future colliders will further test the SM predictions and search for BSM effects.

### III. SEARCH FOR THE HIGGS BOSON

The Higgs boson, while a theoretically essential to the standard model, remained elusive to experimental searches at colliders for a substantial amount of time. In this section, we provide an introduction to the history of Higgs boson searches up until it was discovered at the Large Hadron Collider (LHC) by the ATLAS<sup>2</sup> and CMS<sup>3</sup> experiments in 2012.

#### A. Difficulties involved in Higgs boson searches

The mass of the Higgs boson is not predicted by theory at tree-level. There are constraints that may be put on the available parameter space, for example, through the unitarity of the  $W^+W^- \rightarrow W^+W^-$  process, which requires that the Higgs mass  $m_H \leq \sqrt{4\pi\sqrt{2}/3G_F} \approx 700$  GeV. In addition, we have vacuum stability and triviality arguments, which put a lower and upper bound on the Higgs mass, respectively, at a given energy scale. This is encapsulated in the following graph:

We now explore various experiments leading upto the LHC, in a chronological fashion. We start with Pre-LEP<sup>4</sup> searches.

<sup>2</sup> A Toroidal LHC Apparatus

<sup>3</sup> Compact Muon Solenoid

<sup>4</sup> Large Electron-Positron Collider

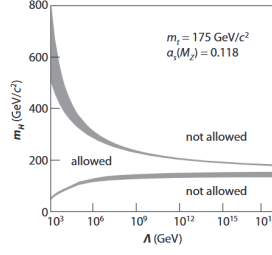


FIG. 4: Lower and upper limits on the Higgs boson mass as a function of the cut-off energy scale  $\Lambda$ , relying on the vacuum stability (lower band) and triviality (upper band) arguments.

### B. Pre-LEP Searches

Before the LEP, the following experiments looked at Higgs masses  $< 5 \text{ GeV}/c^2$  and ruled them unlikely: The SINDRUM spectrometer studied the decay of the pion to an electron, an electron neutrino, and a Higgs boson decaying in turn to a pair of electrons. This

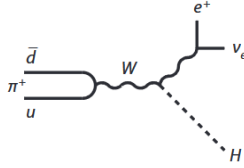


FIG. 5: Process studied by SINDRUM spectrometer.

excluded masses in the range  $10 \text{ MeV}/c^2 < m_H < 110 \text{ MeV}/c^2$  [4]. The CERN-Edinburgh-Mainz-Orsay-Pisa-Siegen collaboration at CERN SPS looked for the decay of a Higgs boson into a pair of electrons  $K_L^0 \rightarrow \pi^0 H$  decay. Negative results excluded  $m_H < 50 \text{ MeV}/c^2$  [5]. An upper limit on the product of the branching ratios  $BR(K_L^0 \rightarrow \pi^0 H) \times BR(H \rightarrow e^+ e^-)$  of  $\approx 2 \times 10^{-8}$  was obtained. CLEO looked at Decays of the Higgs boson

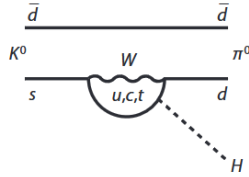


FIG. 6: Process studied by the CERN-EMOPS collaboration at CERN SPS

into a pair of  $\mu\mu, \pi\pi, KK$  through the flavor-changing neutral current decay  $B \rightarrow K^0 H$ . Negative results excluded  $0.2 \text{ GeV}/c^2 < m_H < 3.6 \text{ GeV}/c^2$ . The exclusion was based on a B-to-Higgs-boson branching evaluation, which is subject to a large theoretical uncertainty. Finally, CUSB excluded  $2m_\mu < m_H < 5 \text{ GeV}/c^2$  [6], based on the search for a monochromatic photon sample from

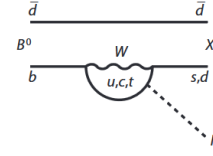


FIG. 7: Decays of the Higgs boson studied by CLEO

the decay  $\Upsilon \rightarrow \gamma + X$ . However, a common thread in

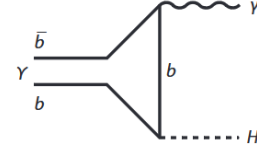


FIG. 8: Radiative decay of the  $\Upsilon$  into a Higgs boson

all these experiments was the possibility of large QCD corrections, which justified the requirement of more significant searches in the low-mass region.

### C. LEP1 Period

The Large Electron-Positron Collider (LEP) was operational at CERN from 1989 to 2000. It was a circular collider with a circumference of 27 kilometers, located in a tunnel beneath the French-Swiss border near Geneva, which now houses the LHC. Especially, relevant for low  $m_H$  searches was the large production cross-section in  $Z$  boson decays, which allowed LEP to further rule out light Higgs masses.

#### 1. Production Mechanisms at the $Z$ Resonance

At LEP1, the Bjorken process  $e^+ e^- \rightarrow H Z^* \rightarrow H f \bar{f}$ , was the dominant production mechanism. An accompanying process was the Wilczek process, involving a top-quark loop,  $e^+ e^- \rightarrow H \gamma$ . However, this process was highly suppressed due to the top-quark loop involved. It was also susceptible to significant backgrounds, owing to processes such as  $e^+ e^- \rightarrow q \bar{q} \gamma$  and  $e^+ e^- \rightarrow q \bar{q} g$ . In these

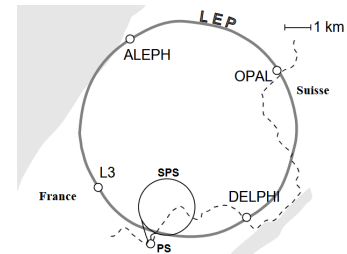


FIG. 9: Overview of the LEP collider

processes, a jet hadronizes into an energetic  $\pi^0$ , greatly reducing any statistical significance of searches through this channel. These processes are depicted in Figure 10.

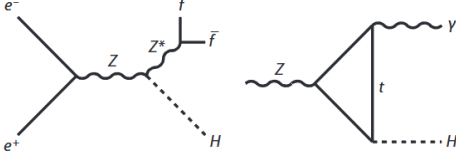


FIG. 10: (left) Bjorken process, (right) Wilczek process

## 2. Low-Mass Searches

Following the analysis in, we may draw up the following table of primary decay channels of the Higgs boson at low masses:

Higgs boson mass range	Primary decay products
$m_H < 2m_e$	$\gamma\gamma$
$2m_e < m_H < 2m_\mu$	$e^+e^-$
$2m_\mu < m_H < 2m_\pi$	$\mu^+\mu^-$
$2m_\pi < m_H < (2 - 3\text{GeV}/c^2)$	hadron pair
PQCD domain $< b\bar{b}$ threshold	heaviest available $f\bar{f}$ ( $c\bar{c}$ or $\tau^+\tau^-$ )
Above $b\bar{b}$ threshold	$b\bar{b}$

This decay into specific particles, owes itself to opening up of different channels as the Higgs mass increases. For example, for very low Higgs mass domain,  $m_H < 2m_\mu$ , the only final states available for the Higgs to decay into are  $e^+e^-$  through the direct Yukawa coupling, and  $\gamma\gamma$  through loop diagrams. As the expected Higgs mass increases, it get other decay topologies that become more significant, with a sudden increase in its branching fraction, as seen in in Figure 11..

It is also noted, however, that for masses higher than  $\sim 2 \text{ GeV}/c^2$ , the branching ratios evolve smoothly (Figure 11). This suggests a transition to perturbative QCD, as the strong coupling constant  $\alpha_s$  heads towards asymptotic freedom. The Higgs boson mass at which transition into the perturbative domain occurs was computed by demanding that branching ratios into strangeness and final-state multiplicities are identical. We get the transition occurring for  $m_H \sim 2 \text{ GeV}/c^2$ .

In the high-mass regime, the branching fractions of the Higgs boson exhibit significant variations, with decays into heavier particles becoming dominant. This behaviour, depicted in Figure 12, is critical for designing efficient search strategies.

For low-mass Higgs scenarios ( $m_H < 20 \text{ GeV}/c^2$ ), over 10,000 events were expected at LEP1 via the Higgsstrahlung process  $e^+e^- \rightarrow Z^* \rightarrow ZH$ . The experimental strategies were tailored to exploit different event

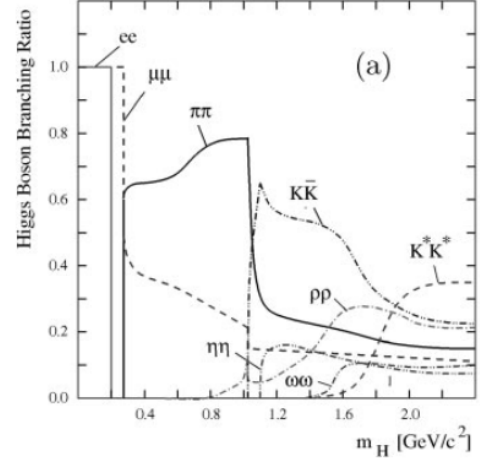


FIG. 11: Branching ratios of Higgs boson for low mass Higgs.

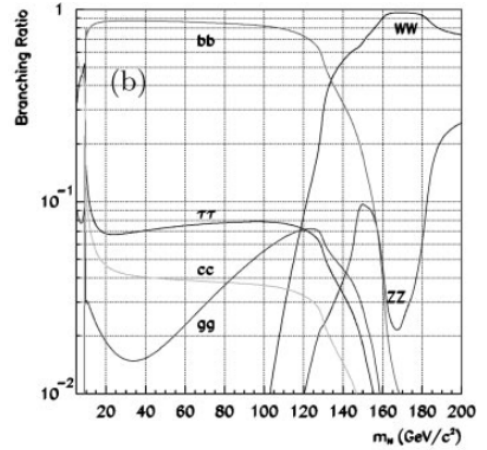


FIG. 12: Higgs boson branching fractions in the heavier mass regime[7]

topologies<sup>5</sup>, including acoplanar lepton pairs<sup>6</sup> from  $Z^*$  decays, acoplanar pairs from missing energy and momentum due to invisible Higgs recoil<sup>7</sup>, and monojet topologies associated with hadronic Higgs decays<sup>8</sup>. Notably, the latter two topologies are significantly affected by background processes such as  $e^+e^- \rightarrow \gamma^* Z \rightarrow \gamma^* \nu\nu$ . The number of observed events showed no significant deviation from the Standard Model (SM) expectations, leading to the exclusion of  $m_H < 20 \text{ GeV}/c^2$  at the 95% confidence level.

<sup>5</sup> Topology in collider physics, generally refers to the signal shape that is detected by a detector, similar to track shapes.

<sup>6</sup> Leptons are assumed to originate from  $Z^*$  decay, a relatively background free channel

<sup>7</sup> Corresponds to decay of  $Z^*$  into a pair of neutrinos

<sup>8</sup> Single jet recoils to a  $Z^*$ , decaying to  $\nu\nu$

Further searches focused on the leptonic decay channels of  $Z^*$ , specifically  $Z^* \rightarrow \nu\nu, \mu\mu, ee$ , due to excessive hadronic backgrounds and the low expected event rates—fewer than 40 events were predicted. These leptonic modes collectively constitute approximately 25% of the decays. Among the approximately 13 million hadronic decays recorded at LEP by all four collaborations, only 10 events were associated with this channel. Despite the limited statistics, combined results established a lower bound on the Higgs mass of  $m_H > 65.6 \text{ GeV}/c^{29}$ .

#### D. LEP2 Period

The LEP2 phase marked a significant upgrade in center-of-mass energy, with  $\sqrt{s}$  reaching 160 GeV in 1996, enabling direct searches for on-shell diboson production via  $e^+e^- \rightarrow ZH$ . By 2000, the machine reached  $\sqrt{s} = 209 \text{ GeV}$ .

##### 1. Signal Characteristics

The dominant Higgs boson production at LEP2 was due to its direct couplings to the  $Z$  and  $W$  bosons. Consequently, the production cross sections are primarily sensitive to the electroweak symmetry breaking sector and not to the Higgs couplings to fermions. The main processes are Higgsstrahlung and vector boson fusion.

Figure 13 illustrates the tree-level Feynman diagrams for these processes, while Figure 14 presents their contributions to the total cross section at  $\sqrt{s} = 206.6 \text{ GeV}$ —the energy of highest statistical significance for the Higgs search—and the total cross section at the maximum LEP energy  $\sqrt{s} = 209 \text{ GeV}$ .

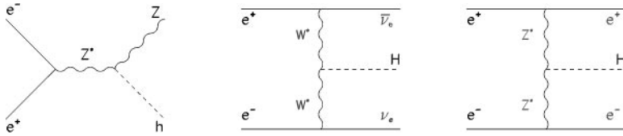


FIG. 13: Diagrams of the Higgsstrahlung and the gauge boson fusion processes of Higgs boson production at LEP2.

A sharp kinematic threshold appears at  $m_{\text{thres}} = \sqrt{s} - m_Z$  (seen in Figure 12), beyond which the cross section declines steeply. Despite the increasing contribution from  $WW$  fusion at higher energies, Higgsstrahlung remains dominant due to the finite  $Z$  width. Thus, the sensitivity of the LEP Higgs search was tightly constrained by the collider's energy and luminosity.

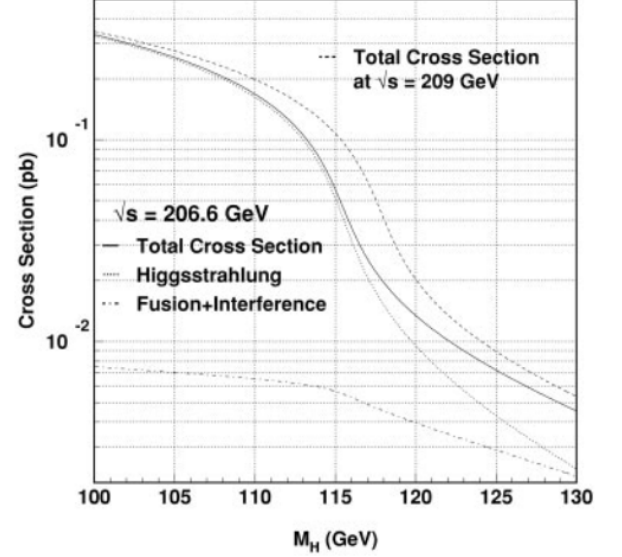


FIG. 14: Contributions to the total cross section for Higgs boson production in  $e^+e^-$  collisions at  $\sqrt{s} = 206.6 \text{ GeV}$ . The total production cross section at  $\sqrt{s} = 209 \text{ GeV}$ , the highest center-of-mass energy achieved at LEP, is also plotted

##### 2. Search Channels

The primary search channels involved were:

- Four-jet channel:** At LEP1, signatures with charged leptons and neutrinos were essential, owing to the overwhelming background in events with hadronic  $Z$  decays. At LEP2, at center-of-mass energies well above the  $Z$  resonance, this particular background was reduced by more than two orders of magnitude. The four-jet channel, because of its higher branching fraction, thus became the most sensitive topology. Higgsstrahlung was the only channel contributing to the 4-jets, resulting in a topology with 2 dijets, one due to the Higgs decay, the other due to the  $Z$  boson decay.
- Missing energy channel:** The Higgsstrahlung process, where the  $Z$  boson decays into a pair of neutrinos and the Higgs boson decays into a  $b\bar{b}$  pair, leads to a distinctive experimental signature: two  $b$ -tagged jets and a large missing mass consistent with the  $Z$  boson mass. This signature also receives contributions from  $W$  boson fusion (see Figure 13). Although constructive interference occurs between the fusion and Higgsstrahlung processes in the  $Z \rightarrow \nu_e \bar{\nu}_e$  final state, the resulting contribution from the interference term is small. Nonetheless, this contribution becomes increasingly relevant near the kinematic threshold for Higgs boson production.

<sup>9</sup> LEP Higgs Working Group, <http://lephiggs.web.cern.ch/LEPHIGGS>



3.  $\ell^+\ell^-$  **channel:** This channel's topologies constrains  $ee, \mu\mu$  and a pair of  $b$ -quark jets. While it is a distinct signature, small branching ratio of the  $Z$  boson decaying into electrons or muons gives it low rates. Additionally, the destructive interference between Higgsstrahlung and  $ZZ$  fusion further suppresses the overall production rate.
4.  $\tau^+\tau^-$  **channel:** Topology contains a pair of tau leptons and a pair of jets. It was treated differently from the  $\ell^+\ell^-$  channel for two primary reasons. First, due to the presence of neutrinos in  $\tau^\pm$  decays, the invariant mass of the  $\tau^+\tau^-$  pair could not be accurately measured, necessitating a distinct reconstruction method similar to that used in the four-jet channel. Second, this channel receives additional contributions from  $Z \rightarrow b\bar{b}$  and  $H \rightarrow ZZ$  decays.

These search channel topologies have been shown in Figure 15.

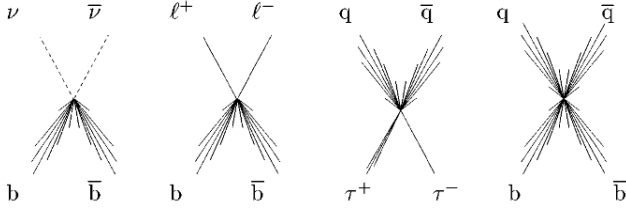


FIG. 15: Topologies involved in the search for the standard-model Higgs boson at LEP2: missing energy, lepton pairs,  $\tau^+\tau^-$ , and four-jet final states [7]

Despite these advances, the Higgs boson eluded discovery at LEP. The measured cross-sections for various  $e^+e^- \rightarrow X$  processes by the L3 collaboration (Figure 16) reveal that  $\sigma(e^+e^- \rightarrow HZ)$  remained small, posing a challenge to observation.

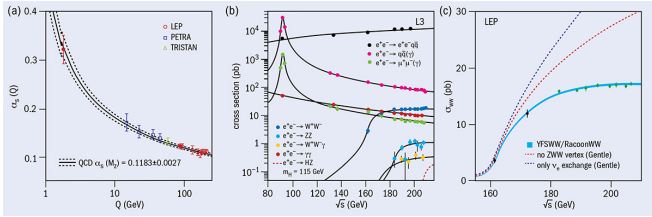


FIG. 16: Measurements of various  $e^+e^- \rightarrow X$  cross sections by L3 at LEP. Note the low cross-section values for Higgs production, in the central plot, indicated by a red-dashed line.

A candidate event collected by the ALEPH detector on June 14, 2000, illustrated four hadronic jets that could potentially originate from  $ZH$  production, with both bosons decaying into quark-antiquark pairs. However, the possibility of such a final state arising from alternative processes renders this evidence inconclusive.

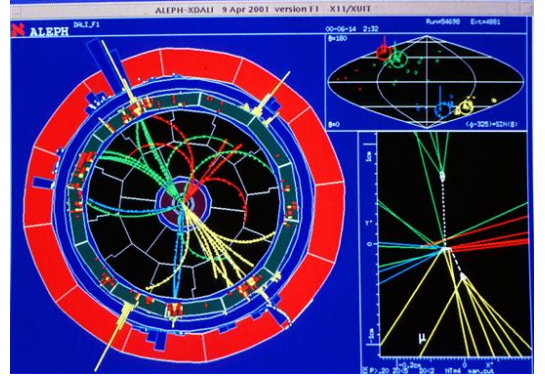


FIG. 17: A four-jet event recorded by ALEPH at LEP. While compatible with  $ZH$  production, the ambiguity in hadronic signatures prevents conclusive identification.

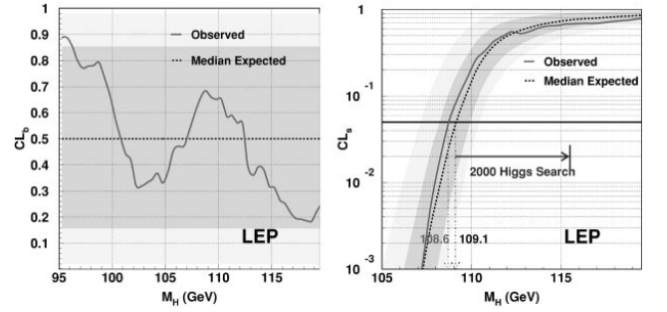


FIG. 18: LEP data up to 2000: as a function of the Higgs boson mass,  $m_H$ , the confidence level for (a) the background and (b) the signal

### 3. Lower limit on the Higgs mass, before 2000

The data collected up to the end of 1999, at center-of-mass energies reaching  $\sqrt{s} = 201.6$  GeV, showed no evidence of Higgs boson production. As shown in Figure 18, the data are consistent with the background-only hypothesis, indicating a good understanding of background processes. The 95% confidence level exclusion limit on the Higgs boson mass is  $m_H = 108.6$  GeV/ $c^2$ , with a median expected limit of 109.1 GeV/ $c^2$ . The sharp decline in  $CL_s$  below 107 GeV/ $c^2$  demonstrates the strong exclusion power in this region. No signal-like excess is observed up to the kinematic limit of approximately 110.4 GeV/ $c^2$ . Following the crossing of the  $ZZ$  production threshold in 1999, the LEP Higgs search program relied on further increases in beam energy and luminosity in 2000.

## E. Indications of the Higgs boson at the Tevatron

Turning to the Tevatron at Fermilab, although a definitive discovery was not achieved, the experiments observed significant excesses suggestive of the Higgs boson[8]



The *CDF* and *D0* collaborations analyzed data from  $p\bar{p}$  collisions at  $\sqrt{s} = 1.96$  TeV, with integrated luminosities up to  $9.7 \text{ fb}^{-1}$ . Searches were conducted in the mass range  $100\text{--}150 \text{ GeV}/c^2$ , with an excess observed between 120 and 135  $\text{GeV}/c^2$  corresponding to a global significance of  $3.1\sigma$  (see Figure 19).

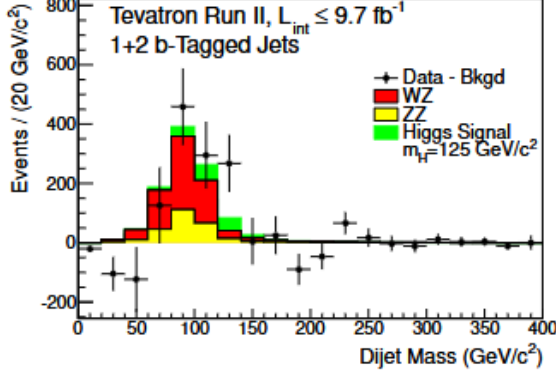


FIG. 19: Background-subtracted distribution of the reconstructed dijet mass  $m_{jj}$ , summed over all input channels[8]

While the significance of the excess did not reach discovery threshold, the results were limited by statistical power. As shown in Figure 20, despite steadily increasing, the peak luminosities simply were insufficient to yield a higher significance.

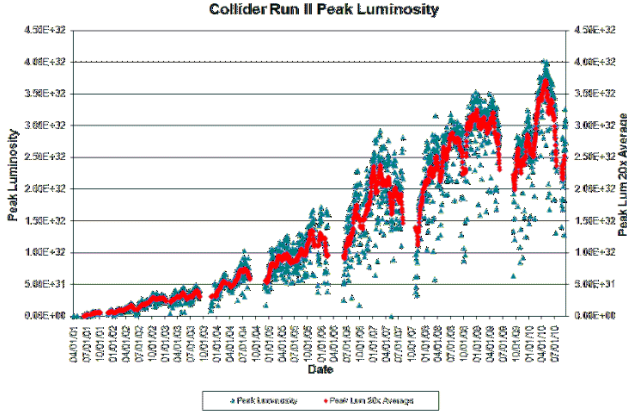


FIG. 20: Increase in peak luminosities of the Tevatron over time.

Another important factor in non-clean signals for the Higgs, was the nature of its decays. At  $m_H = 125 \text{ GeV}/c^2$ , the dominant decay channel is  $H \rightarrow b\bar{b}$  (see Figure 21). However, this mode is difficult to isolate in a hadron collider environment due to the overwhelming background and poor resolution of hadronic jets. Again, there was a lack of adequate data to enhance statistical significance of the presence of a Higgs boson in the Teva-

tron. A point to note is that, as seen in Figure 22, even LHC searches in the  $H \rightarrow b\bar{b}$  channel (produced as  $VH$ ) fail to attain the requisite  $5\sigma$  significance required for a conclusive discovery.

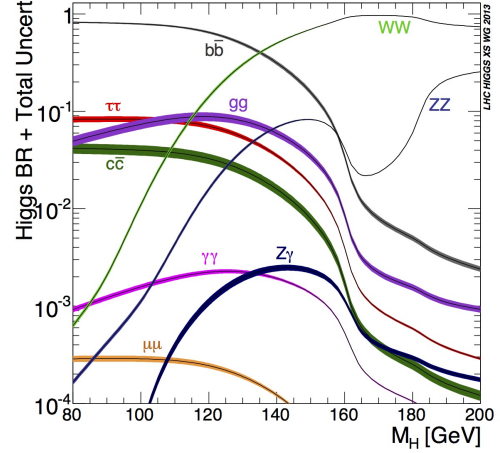


FIG. 21: Branching ratios of the Higgs boson as a function of  $m_H$ [9]

Experiment	$\mu = \sigma/\sigma_{\text{SM}}$	Expected significance
CDF	$2.5 \pm 1.0$	$1.3 \sigma$ [17]
D0	$1.2 \pm 1.1$	$1.5 \sigma$ [18]
D0+CDF	$1.95 \pm 0.75$	$1.9 \sigma$ [16]
ATLAS	$0.2 \pm 0.9$	$1.6 \sigma$ [19]
CMS	$1.0 \pm 0.5$	$2.1 \sigma$ [8]

FIG. 22: Signal strength and expected significance for  $VH$  searches at Tevatron and LHC[10]

Jets from  $b$ -quarks are not clean signatures. In hadron colliders like the Tevatron, the immense QCD background complicates signal extraction. To address this, experiments instead target rarer but cleaner decay modes such as  $H \rightarrow ZZ$  and  $H \rightarrow \gamma\gamma$ , with branching ratios of 2.67% and 0.228%, respectively. However, the Tevatron lacked the luminosity to fully exploit these channels. This limitation marked the transition to LHC-based searches.

## F. The LHC and the Discovery of the Higgs

The Large Hadron Collider (LHC) is the world's largest and most powerful particle accelerator. Situated at CERN, it utilizes a series of accelerators in a complex layout to bring protons up to energies of several TeV before collisions occur in detectors such as ATLAS and CMS. A schematic overview of the accelerator complex is shown in Figure 23.

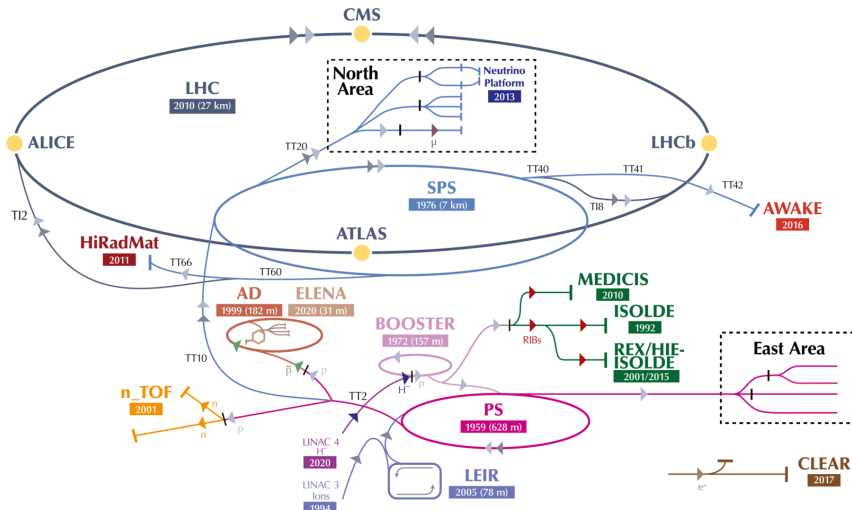


FIG. 23: The CERN accelerator complex layout in 2022 [11].

### 1. The ATLAS Experiment

The ATLAS experiment[12] at the LHC is a general-purpose particle detector featuring a forward-backward symmetric, cylindrical geometry with nearly full  $4\pi$  solid angle coverage. Its cylindrical shape measures 46 meters in length and 25 meters in diameter, and is located 100 meters underground. Its total weight is approximately 7,000 tonnes, comparable to the Eiffel Tower (Figure 24).

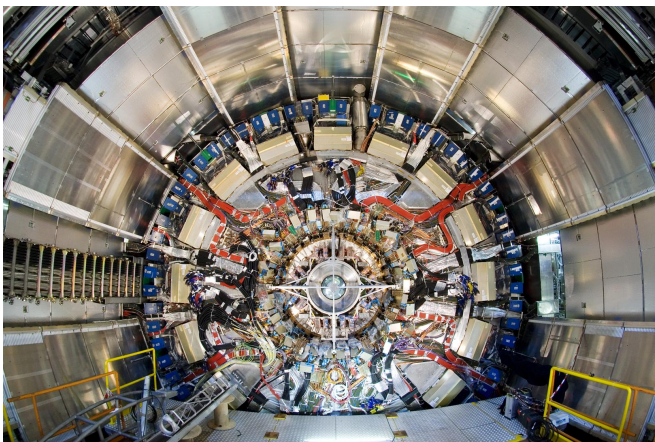


FIG. 24: The ATLAS detector at the LHC.

ATLAS collects digitized signals from proton-proton collision products, referred to as collision *events*. It can identify a wide range of particles and measure their momenta and energies, including that of electrons, muons,  $\tau$ -leptons, photons, as well as gluons and quarks, which manifest as collimated *jets*. Jets originating from  $b$ - and  $c$ -quarks can be identified by displaced decay vertices due to the relatively long lifetimes of hadrons containing these quarks. Invisible particles, such as neutrinos,

are inferred via an imbalance in the vector sum of transverse momenta of visible particles, assuming momentum conservation.

Charged-particle tracking and momentum measurements are performed by the inner detector, located closest to the interaction point. This is surrounded by calorimeters that enable energy measurement and particle identification, and in turn by a muon spectrometer that tracks muons—the only charged particles capable of traversing the calorimeters. While we will now discuss ATLAS with respect to the Higgs discovery time period (2012), it is useful to know that with time, a two-level trigger system, optimized for Run 2 data-taking, has allowed selection of events of interest at a rate of  $\sim 1$  kHz from all the events, which occur at  $\sim 40$  MHz. A comprehensive software framework[13] is employed for detector operation, data acquisition, event reconstruction, and the analysis of both real and simulated events.

It is also useful to know some terminology relevant in collider physics. Collisions at the LHC occur in bunches of about  $10^{11}$  protons, squeezed to a transverse size of around 64 microns at the interaction point. Bunches cross every 25 ns, resulting in multiple interactions per *bunch crossing*—a phenomenon known as *pileup* (Figure 25).

A key reason for using bunched beams in particle accelerators lies in the nature of RF (radio frequency) acceleration. Linear accelerators (linacs) employ a series of resonant cavities powered by a high-power RF source, such as a klystron, which produces oscillating electric fields in the form of standing waves along the beam axis. To achieve efficient acceleration, particle bunches must enter each cavity at a precise phase of the oscillating electric field. The spacing between cavities is carefully designed so that particles traverse drift tubes and enter subsequent cavities at the correct phase, ensuring continuous acceleration throughout the linac. A continuous

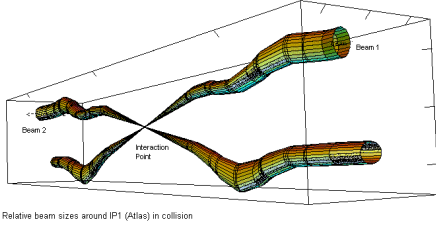


FIG. 25: Bunch crossing/pileup in ATLAS: protons per bunch and bunch crossing rate. IP1 indicates high luminosity point present in the detector.

beam would fail to maintain synchronization with the RF field, resulting in inefficient or even decelerating interactions. RF-based acceleration is preferred over static fields because it enables higher accelerating gradients for a given power input, making it a more energy-efficient and practical solution.

We now do a back-of-the-envelope calculation to see where the 40 MHz event rate arises from. By definition, the event rate is given by

$$\text{Event rate} = \mathcal{L} \times \sigma, \quad (61)$$

where  $\mathcal{L}$  is the instantaneous luminosity and  $\sigma$  the interaction cross section.

At  $\sqrt{s} = 7$  TeV, the total proton-proton cross section is approximately 110 mb, decomposed as:

- Inelastic:  $\sigma_{\text{inel}} \approx 60$  mb,
- Single diffractive:  $\sigma_{\text{sd}} \approx 12$  mb,
- Elastic:  $\sigma_{\text{el}} \approx 40$  mb.

Only inelastic collisions produce particles at large enough angles to be detected. At the nominal luminosity of  $10^{34} \text{ cm}^{-2}\text{s}^{-1}$ , the inelastic event rate is

$$10^{34} \times 60 \times 10^{-3} \times 10^{-24} = 6 \times 10^8 \text{ events/s}, \quad (62)$$

corresponding to approximately 19 inelastic events per bunch crossing.

With a bunch spacing of  $\sim 25$  ns, the peak crossing rate is 40 MHz. Accounting for gaps, the average crossing rate becomes

$$2808 \text{ bunches} \times 11.245 \text{ kHz} \approx 31.6 \text{ MHz}, \quad (63)$$

which still yields around 600 million inelastic events per second at design luminosity.

In collider physics, it is often convenient to describe angular distributions in terms of pseudorapidity  $\eta$ , defined as

$$\eta = -\ln \left[ \tan \left( \frac{\theta}{2} \right) \right], \quad (64)$$

where  $\theta$  is the polar angle<sup>10</sup> from the beam axis (see Figure 26). Pseudorapidity is a measure of the angle between the beam axis and the particle's momentum. We shall see that it may be used, along with the polar angle  $\phi$ , to describe an invariant quantity called  $\Delta R$ .

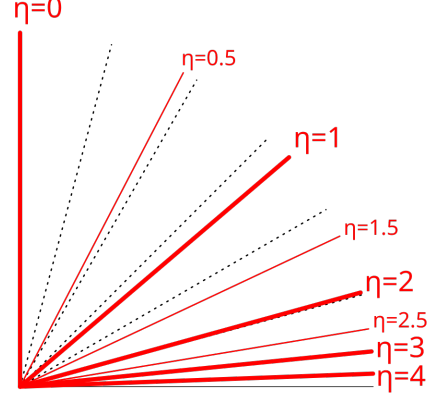


FIG. 26: Definition of pseudorapidity  $\eta$ .

We now describe components of the ATLAS detector. The inner detector (ID), consisting of a silicon pixel detector, a silicon microstrip tracker (SCT), and a straw-tube transition radiation tracker (TRT), is enclosed within a 2 T solenoidal magnetic field. Surrounding the ID is a high-granularity liquid-argon (LAr) sampling electromagnetic calorimeter, segmented into a central barrel ( $|\eta| < 1.475$ ) and end-cap regions ( $1.375 < |\eta| < 3.2$ ), with fine  $\eta$  segmentation in the first layer for enhanced  $e/\gamma$  identification. A presampler is used in the region  $|\eta| < 1.8$  to correct for upstream energy losses. Hadronic calorimetry in the central region ( $|\eta| < 1.7$ ) is provided by an iron-scintillator tile calorimeter, while LAr hadronic end-caps cover  $1.5 < |\eta| < 3.2$ . Forward calorimeters extend the coverage to  $|\eta| < 4.9$ . The muon spectrometer (MS), consisting of air-core toroidal magnets and precision tracking chambers, surrounds the calorimeters. The full system enables accurate tracking and efficient identification of leptons, photons, jets for  $|\eta| < 2.5$  and missing transverse energy over the full pseudorapidity range ( $|\eta| < 4.9$ ).

<sup>10</sup> ATLAS uses a right-handed coordinate system with its origin at the nominal interaction point (IP) in the centre of the detector, and the z-axis along the beam line. The x-axis points from the IP to the centre of the LHC ring, and the y-axis points upwards. Cylindrical coordinates  $(r, \phi)$  are used in the transverse plane,  $\phi$  being the azimuthal angle around the beam line. Observables labelled “transverse” are projected into the x–y plane.

## 2. Indication of the Higgs boson at the LHC

By December 12, 2011, ATLAS reported first hints of an excess in invariant mass distributions potentially corresponding to the Higgs boson (Figure 27). These were followed up by more detailed analyses in early 2012.

On February 7, 2012, ATLAS published a more detailed report[14]. Gluon-gluon fusion was identified as the dominant production mode, and searches were carried out in the channels  $H \rightarrow \gamma\gamma$ ,  $H \rightarrow ZZ^* \rightarrow 4\ell$ ,  $H \rightarrow ZZ \rightarrow \ell\ell q\bar{q}$ ,  $H \rightarrow ZZ \rightarrow \ell\ell\nu\bar{\nu}$ , and  $H \rightarrow WW^* \rightarrow \ell\nu\ell'\nu'$ . These revealed a local excess of events near  $m_H = 126$  GeV.

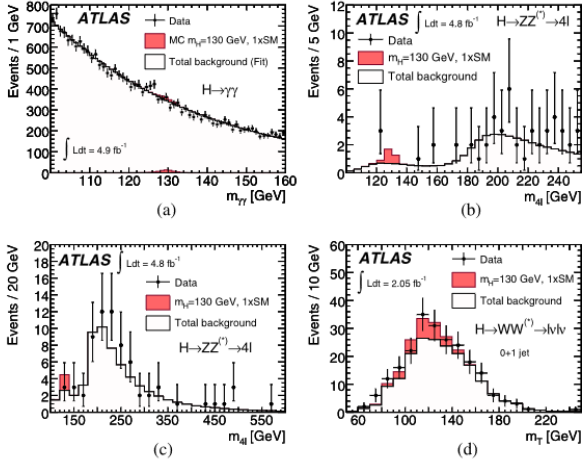


FIG. 27: Reconstructed invariant/transverse mass distributions in  $H \rightarrow \gamma\gamma$ ,  $H \rightarrow ZZ^* \rightarrow 4\ell$ , and  $H \rightarrow WW^* \rightarrow \ell\nu\ell'\nu'$  channels.

After further data collection and analysis, the discovery was officially announced on July 4, 2012. A statistically significant excess was seen in the relevant channels, that we shall now describe.

## 3. Production mechanisms

The SM Higgs boson production processes considered in this analysis are the dominant gluon fusion ( $gg \rightarrow H$ , denoted ggF), vector-boson fusion ( $qq' \rightarrow qq' H$ , denoted VBF) and Higgs-strahlung ( $qq' \rightarrow WH, ZH$ , denoted WH/ZH) (see Figure 28). The small contribution from the associated production with a  $t\bar{t}$  pair ( $q\bar{q}/gg \rightarrow t\bar{t}H$ , denoted  $t\bar{t}H$ ) is taken into account only in the  $H \rightarrow \gamma\gamma$  analysis.

For the ggF process, the signal cross section is computed at up to next-to-next-to-leading order (NNLO) in QCD. Next-to-leading order (NLO) electroweak (EW) corrections are applied, as well as QCD soft-gluon resummations at up to next-to-next-to-leading logarithm (NNLL). These calculations assume factorisation between QCD and EW corrections. The transverse momen-

tum,  $p_T$ , spectrum of the Higgs boson in the ggF process follows the HqT calculation, which includes QCD corrections at NLO and QCD soft-gluon re-summations up to NNLL; the effects of finite quark masses are also taken into account. For the VBF process, full QCD and EW corrections up to NLO and approximate NNLO QCD corrections are used to calculate the cross section. Cross sections of the associated WH/ZH processes (VH) are calculated including QCD corrections up to NNLO and EW corrections up to NLO. The cross sections for the  $t\bar{t}H$  process are estimated up to NLO QCD. The total cross sections for SM Higgs boson production at the LHC with  $m_H = 125$  GeV are predicted to be 17.5 pb for  $\sqrt{s} = 7$  TeV and 22.3 pb for  $\sqrt{s} = 8$  TeV. These predictions are shown in Figure 29

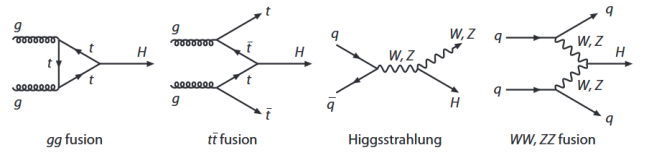


FIG. 28: Standard Model Higgs boson production processes considered in the analysis.

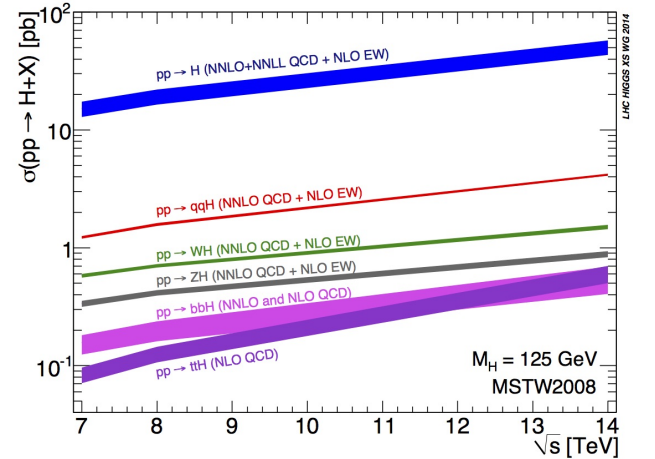


FIG. 29: SM cross sections expected for Higgs production mechanisms with relevant correction mentioned.[9].

Branching ratios of the SM Higgs boson were calculated using HDECAY and PROPHECY4F programs. The interference in  $h \rightarrow ZZ^* \rightarrow 4\ell$  final states with identical leptons was also taken into account.

A table of Monte-Carlo simulators and event generators utilised to background both signal and background processes is attached in Figure 30. Full simulations of the ATLAS detector using GEANT4 were conducted, which involved a realistic modelling of the pile-up conditions present in the system.



**Table 1**

Event generators used to model the signal and background processes. “PYTHIA” indicates that PYTHIA6 and PYTHIA8 are used for simulations of  $\sqrt{s} = 7$  TeV and  $\sqrt{s} = 8$  TeV data, respectively.

Process	Generator
ggF, VBF $WH, ZH, t\bar{t}H$	POWHEG [57,58] + PYTHIA PYTHIA
$W$ + jets, $Z/\gamma^* + \text{jets}$ $t\bar{t}, tW, tb$ $tqb$	ALPGEN [59] + HERWIG MC@NLO [60] + HERWIG AcerMC [61] + PYTHIA
$q\bar{q} \rightarrow WW$ $gg \rightarrow WW$ $q\bar{q} \rightarrow ZZ$ $gg \rightarrow ZZ$ $WZ$	MC@NLO + HERWIG gg2WW [62] + HERWIG POWHEG [63] + PYTHIA gg2ZZ [64] + HERWIG MadGraph + PYTHIA, HERWIG
$W\gamma$ + jets $W\gamma^*$ [65] $q\bar{q}/gg \rightarrow \gamma\gamma$	ALPGEN + HERWIG MadGraph + PYTHIA SHERPA

FIG. 30: Simulation and Monte Carlo tools used for Higgs searches.

#### 4. Event Selection

We will now, give a basic overview of different event selection criteria employed for the analysis of the Higgs decay channels under consideration. The exact details are present in the original ATLAS paper declaring the discovery of the Higgs boson[15], and may be referred to.

##### a. $H \rightarrow ZZ^{(*)} \rightarrow 4\ell$ channel

The analysis of the  $H \rightarrow ZZ^{(*)} \rightarrow 4\ell$  decay channel uses single-lepton and dilepton triggers with varying  $p_T$  and  $E_T$  thresholds for 7 TeV and 8 TeV data. Electron and muon candidates are reconstructed using combinations of tracking and calorimeter information, with acceptance up to  $|\eta| < 2.47$  for electrons and  $|\eta| < 2.7$  for muons. Leptons must meet isolation and impact parameter requirements to suppress non-prompt backgrounds. Events are required to contain four leptons forming opposite-charge, same-flavour pairs. The leading pair invariant mass must lie within 50–106 GeV, while the sub-leading pair must fall in a mass window dependent on the four-lepton invariant mass. Only one quadruplet per event is selected based on the highest sub-leading pair mass.

To reduce backgrounds from  $Z$ +jets and  $t\bar{t}$  processes, selection includes cuts on impact parameter<sup>11</sup> significance and track and calorimetric isolation. Final signal efficiencies for  $m_H = 125$  GeV range from 15–37% across the  $4e$ ,  $2e2\mu/2\mu2e$ , and  $4\mu$  channels. Mass resolution is enhanced via a  $Z$ -mass-constrained kinematic fit. For  $m_H = 125$  GeV, the typical four-lepton invariant mass resolution is 1.7–2.3 GeV, with experimental resolution dominating below 350 GeV.

<sup>11</sup> Here impact parameter is defined as distance of closest approach of to the primary vertex in the transverse plane. Also, the primary vertex is defined differently for different events, in this case, it is the vertex with highest  $\Sigma p_T^2$

b.  $H \rightarrow \gamma\gamma$  channel Events are selected using a diphoton trigger, which requires two clusters in the electromagnetic calorimeter. For the 7 TeV dataset, each cluster must have transverse energy  $E_T > 20$  GeV. For the 8 TeV dataset, the leading and sub-leading clusters must satisfy  $E_T > 35$  GeV and  $E_T > 25$  GeV, respectively. In both cases, clusters must also pass loose shower shape criteria consistent with electromagnetic showers initiated by photons. The trigger efficiency exceeds 99% for events passing the final selection.

Selected events must contain at least one reconstructed vertex with two or more associated tracks of  $p_T > 0.4$  GeV, and two photon candidates within the fiducial region  $|\eta| < 2.37$ , excluding the barrel–endcap transition region  $1.37 < |\eta| < 1.52$ . Photon candidates may be either unconverted or converted, the latter having one or two tracks matched to calorimeter clusters. The photon reconstruction efficiency is approximately 97% for  $E_T > 30$  GeV.

Photon energies are calibrated using Monte Carlo (MC) simulations to account for energy losses upstream of the calorimeter and leakage outside the cluster. Separate calibrations are applied for converted and unconverted photons. Further  $\eta$ -dependent corrections of the order of  $\pm 1\%$  are derived using  $Z \rightarrow e^+e^-$  events. The final selection requires the leading (sub-leading) photon to have  $E_T > 40$  GeV (30 GeV).

Photon identification is based on shower shape variables in the electromagnetic calorimeter and energy leakage into the hadronic calorimeter. For the 7 TeV data, these inputs are combined using a neural network optimized for jet rejection and high photon efficiency. For the 8 TeV data, a cut-based approach is used to ensure robustness against pile-up by relaxing criteria sensitive to pile-up and tightening others. The identification efficiency, averaged over  $\eta$ , ranges from 85% to over 95% in the relevant  $E_T$  range.

To suppress the jet background, an isolation requirement is applied. The isolation transverse energy is defined as the sum of transverse energy in positive-energy topological clusters, within a cone of  $\Delta R = 0.4$ <sup>12</sup> around the photon candidate, excluding a core region of size  $0.125 \times 0.175$  in  $\eta \times \phi$  around the photon barycentre. The data and simulation distributions of isolation transverse energy agree well, as verified using electrons from  $Z \rightarrow e^+e^-$  events and photons from  $Z \rightarrow \ell^+\ell^-\gamma$  events. Residual differences are treated as a systematic uncertainty. Photon candidates are required to have isolation  $E_T < 4$  GeV.

c.  $H \rightarrow WW^{(*)} \rightarrow e\nu\mu\nu$  channel The  $H \rightarrow WW^{(*)} \rightarrow e\nu\mu\nu$  search at  $\sqrt{s} = 8$  TeV uses inclusive single-lepton triggers requiring an isolated lepton with  $p_T > 24$  GeV. Events with two opposite-charge, different-flavour leptons are selected, with  $p_T > 25$  GeV

<sup>12</sup>  $(\Delta R)^2 = (\Delta\eta)^2 + (\Delta\phi)^2$

for the leading lepton and  $> 15$  GeV for the sub-leading one. To reduce backgrounds, stringent lepton identification and isolation criteria are imposed, along with requirements on missing transverse energy,  $E_T^{\text{miss,rel}} > 25$  GeV. Events are categorised into 0-, 1-, and 2-jet bins, with additional kinematic selections to suppress backgrounds like Drell-Yan and  $t\bar{t}$ . The  $\Delta\phi_{\ell\ell} < 1.8$  and low dilepton mass  $m_{\ell\ell}$  further exploit spin correlations in signal events.

The 2-jet category includes vector boson fusion (VBF) selection criteria: tag jets must have  $|\Delta y_{jj}| > 3.8$ ,  $m_{jj} > 500$  GeV, and no additional jets between them. A transverse mass  $m_T$  variable is used for the final signal extraction via a shape-based fit. For a Higgs mass of 125 GeV, the  $\sigma \times \text{BR}$  to  $e\nu\mu\nu$  is 112 fb. The acceptance times efficiency is approximately 7.4% for 0- and 1-jet ggF events and 14% for 2-jet VBF events prior to the final  $m_T$  selection.

### 5. Backgrounds and estimation strategies

Backgrounds were estimated using both Monte Carlo and data-driven techniques. We give a general overview of the kind of backgrounds taken into consideration.

For the  $H \rightarrow ZZ^{(*)} \rightarrow 4\ell$  channel, the background yield and composition are estimated using MC simulations normalized to the  $ZZ^{(*)}$  cross section and data-driven methods for  $Z$  + jets and  $t\bar{t}$  processes. Separate strategies are used for  $\ell\ell + \mu\mu$  and  $\ell\ell + ee$  final states. Transfer factors from MC extrapolate yields from control to signal regions, with efficiencies validated in data. For  $\ell\ell + \mu\mu$ , a control region is defined by relaxing isolation and requiring at least one sub-leading muon to fail the impact parameter cut, enabling a fit to  $m_{12}$ <sup>13</sup> to estimate  $t\bar{t}$  and  $Z$  + jets backgrounds. A cross-check uses events with an opposite-charge  $e\mu$  pair and a muon pair, excluding  $Z \rightarrow \ell\ell$  candidates. For  $\ell\ell + ee$ , a control region is formed by loosening sub-leading electron selection, and background sources are categorized using discriminating variables. Cross-checks with same-charge electron pairs confirm consistency.

We will not delve into the specifics of background estimation in case of the  $H \rightarrow \gamma\gamma$  and  $H \rightarrow WW^{(*)} \rightarrow e\nu\mu\nu$  channels. Similar to the 4-lepton channel, background estimation involves an elaborate classification scheme (for photons, in case of  $H \rightarrow \gamma\gamma$ , depending upon track shapes, shower reconstruction and so forth), which are not relevant to our discussions currently. Simulation software utilised in such cases were MCFM, MC@NLO + HERWIG, POWHEG + PYTHIA, MadGraph LO and others.

<sup>13</sup>  $m_{12}$  is the invariant mass of the leading lepton pair, which is defined as the same-flavour and opposite-charge lepton pair with an invariant mass closest to the Z boson mass. Similarly,  $m_{34}$  is the invariant mass of the other lepton pair

## G. Final Data and Observations

The final observed invariant mass distributions in the three channels are shown in Figure 31. These plots exhibit clear excesses consistent with Higgs boson decays.

## H. Combined Analysis and Higgs Mass Measurement

The local  $p_0$ -value as a function of Higgs mass  $m_H$  is shown in Fig. 32. The combined data from all channels led to a statistically significant observation.

## I. Conclusive Results

The ATLAS collaboration provided strong evidence for the discovery of a new boson with mass

$$m_H = 126.0 \pm 0.4(\text{stat}) \pm 0.4(\text{sys}) \text{ GeV}.$$

The decay into pairs of vector bosons confirmed the particle's charge neutrality. Furthermore, the diphoton channel ruled out the spin-1 hypothesis, consistent with a scalar boson.

**CMS Collaboration:** Simultaneously reported the discovery with a mass

$$m_H = 125.3 \pm 0.4(\text{stat}) \pm 0.5(\text{sys}) \text{ GeV}.$$

**Combined ATLAS and CMS Measurements (2015)[16]:**

$$m_H = 125.09 \pm 0.21(\text{stat}) \pm 0.11(\text{sys}) \text{ GeV}.$$

This measurement agrees well with Standard Model predictions and supports the overall consistency and stability of electroweak theory.

## IV. HIGGS BOSON INTERACTION MAP AND MEASUREMENTS

We now delve into various fundamental properties of the Higgs and methods employed to probe them. Such experiments are essential in checking the validity of the standard model and discrepancies between theoretical expectations and experimental results indicate the possibility of new physics.

Figure 38 shows a list of primary processes (Higgs production mechanisms as well as decays) studied by ATLAS currently[17]. The dominant Higgs production mechanism remains ggF accounting for roughly 87% of all Higgs production. VBF follows, contributing about 7%, and production in association with a weak boson (Higgstrahlung, with  $W$  or  $Z$ ), contributing 4%. Higher

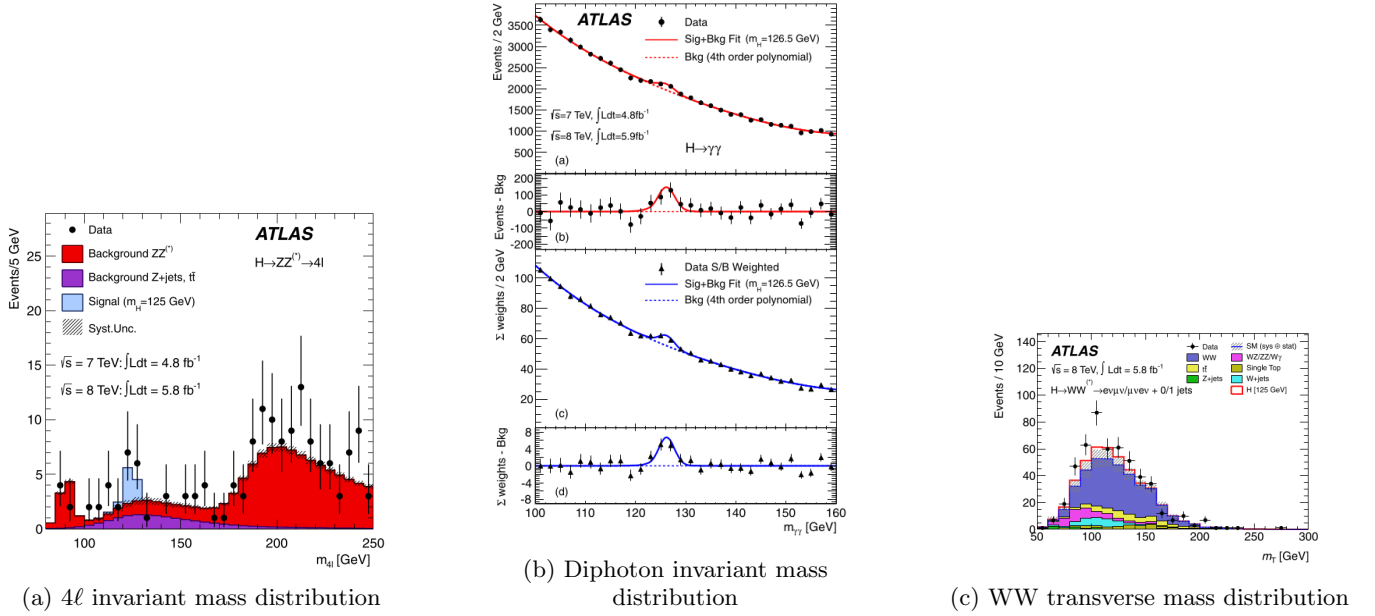
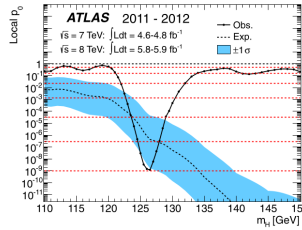


FIG. 31: Final reconstructed mass distributions in each decay channel.

FIG. 32: Observed local  $p_0$  as a function of  $m_H$ , indicating signal significance.

luminosities allow us to also probe, to a higher statistical significance, rarer mechanisms like  $t\bar{t}H$  or  $b\bar{q} \rightarrow t\bar{b}H$  production (each about 1%). Other quark antiquark fusion processes remain experimentally inaccessible. Higgs production with a single top quark is extremely rare, occurring only about 0.05% of the time.

The Higgs has a short lifetime of  $\approx 1.6 \times 10^{-22}$  seconds. 90% of these decays occur through eight primary modes. These modes include decays into a pair of  $b$ -quarks (58%), followed by  $W$  bosons (22%),  $\tau$  leptons (6%),  $c$ -quarks (3%),  $Z$  bosons (3%), photons  $\gamma$  (0.2%), and muons  $\mu$  (less than 0.2%). Additionally, searches are ongoing for possible decays into invisible particles, which could hint at physics beyond the Standard Model, such as the presence of dark matter particles that do not interact with the detector.

### A. Input Measurements

Cross section measurements and decays branching ratios are measured through standard event counting

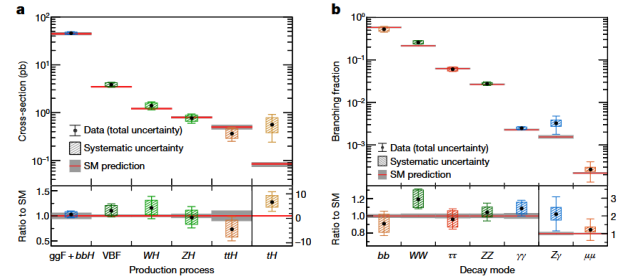


FIG. 33: Production rates and decay branching ratios, and their ratios to SM expectations. The p-values for SM compatibility are: (a) 65%, (b) 56%.

methods (total number of events = cross-section( $\sigma$ )  $\times$  luminosity( $\mathcal{L}$ )). Ratios of measured production rates at the LHC to standard model predictions are shown in figure 33. Clearly, ratios are in the vicinity of unity, including relevant uncertainties, displaying the validity of the standard model. To extract Higgs interaction strengths, simultaneous fits are performed using a set of complementary measurements, weighted by factors such as selection efficiency, signal rates, signal-to-background ratios, and systematic uncertainties.

Event classification, generally based on machine learning techniques, enables discrimination of Higgs production processes for each decay mode. Analyses generally consider contributions from ggF, VBF, Higgstrahlung and production with top-quark pairs ( $t\bar{t}H$ ) or a single top quark ( $tH$ ). Further classification exploits kinematic features of the Higgs boson and associated particles.

Combined measurement use the decay channels that were involved in Higgs searches previously:  $H \rightarrow ZZ \rightarrow$

$\ell^+\ell^-\ell^+\ell^-$ ,  $H \rightarrow WW \rightarrow \ell\nu\ell\nu$ , and  $H \rightarrow \gamma\gamma$ .  $H \rightarrow \gamma\gamma$  is the only channel utilised to discriminate between the  $t\bar{t}H$  and  $tH$  processes. A new search for the rare  $H \rightarrow Z\gamma \rightarrow \ell^+\ell^-\gamma$  decay is included.

Decays to fermions are extensively studied. As mentioned previously, the primary  $H \rightarrow b\bar{b}$  mode involves large backgrounds, but is accessible via  $WH$ ,  $ZH$ , VBF, and  $t\bar{t}H$  channels. A new contribution comes from *boosted*  $H \rightarrow b\bar{b}$  events<sup>14</sup>, offering sensitivity to ggF production. The  $H \rightarrow \tau^+\tau^-$  analysis now includes  $VH$  and combined  $t\bar{t}H/tH$  production. Multilepton final states also contribute, providing sensitivity to  $\tau^+\tau^-$ ,  $WW$ , and  $ZZ$  decays.

Second-generation fermion couplings are probed through  $H \rightarrow \mu^+\mu^-$  and, for the first time,  $H \rightarrow c\bar{c}$ , the latter accessible only via  $WH$  and  $ZH$ . Invisible decays are searched for in VBF and  $ZH$  channels.

Note that data analyses are performed on *full* Run-2 data, with a few exceptional studies, utilise partial Run-2 datasets. For context, Run-2 data refers to the dataset collected by the LHC during its second operational period (2015–2018), following a major upgrade after Run-1 (2010–2012). Run-2 featured proton-proton collisions at

a center-of-mass energy of  $\sqrt{s} = 13$  TeV. This massively increased the availability of data to us, and often gives up to 50% higher sensitivities than older datasets[17].

## B. Signal Strength

The Higgs boson production rates are determined via a likelihood fit to the observed signal yields. Since the production cross section  $\sigma_i$  and the branching fraction  $B_f$  for a given production process  $i$  and decay mode  $f$  cannot be independently measured without additional assumptions, the observed signal yield is expressed in terms of a single signal-strength modifier. The ATLAS collaboration defines the *signal strength modifier*  $\mu_{if}$  for a production process  $i$  and decay channel  $f$  as:

$$\mu_{if} = \frac{\sigma_i}{\sigma_i^{\text{SM}}} \times \frac{B_f}{B_f^{\text{SM}}} \quad (65)$$

In this equation ‘SM’ refers to standard model predictions. Assuming all processes share a global signal strength  $\mu = \mu_{if}$ , the ATLAS measurement yields, for the inclusive Higgs boson production rate, given below.

$$\mu = 1.05 \pm 0.06 = 1.05 \pm 0.03 \text{ (stat)} \pm 0.03 \text{ (exp)} \pm 0.04 \text{ (sig. th)} \pm 0.02 \text{ (bkg. th)} \quad (66)$$

The total measurement uncertainty is decomposed into components for statistical uncertainties, experimental systematic uncertainties, and theory uncertainties in both signal and background modelling. Both the experimental and the theoretical uncertainties are almost a factor of two lower than in the Run 1 result[18]. The signal strength value lies in agreement with the standard model.

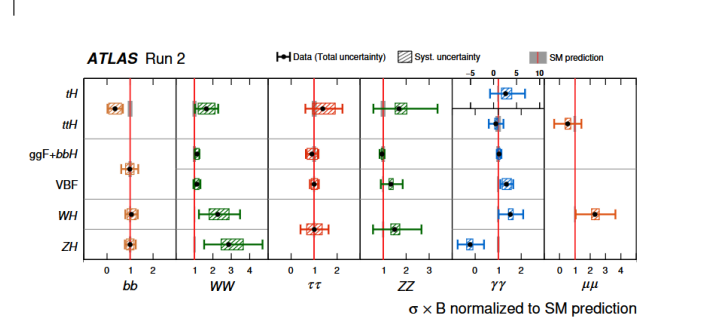


FIG. 34: Ratio of observed to predicted SM event rates for different combinations of Higgs boson production and decay processes.

## C. Higgs Boson Coupling Strength

To extract specific Higgs boson coupling strengths, a simultaneous fit across multiple production and decay measurements is performed within the  $\kappa$ -framework [19]. In this approach, the cross section times branching fraction is expressed using coupling strength modifiers  $\kappa$  that scale Standard Model couplings without modifying kinematic distributions. Each modifier  $\kappa_p$  is defined by  $\kappa_p^2 = \sigma_p/\sigma_p^{\text{SM}}$  or  $\kappa_p^2 = \Gamma_p/\Gamma_p^{\text{SM}}$ , depending on whether it relates to production or decay. The total width includes

<sup>14</sup> “Boosted”  $H \rightarrow b\bar{b}$  events refer to Higgs bosons produced with high transverse momentum, causing their decay products (two  $b$ -quarks) to be emitted close together. These quarks form a single large-radius jet with identifiable substructure. Such events improve signal-to-background discrimination and are useful for probing Higgs decays in challenging environments.



contributions from all known and possible undetected or non-SM decay modes.

Three model classes with increasing generality are considered for Higgs coupling strength fits. Couplings to first-generation fermions are fixed to their SM values, and second-generation quark modifiers are set equal to those of the third generation, except when  $\kappa_c$  is treated freely. Loop-induced processes like ggF,  $H \rightarrow \gamma\gamma$ , and  $H \rightarrow Z\gamma$  are either parameterized using fundamental SM couplings or effective modifiers  $\kappa_g$ ,  $\kappa_\gamma$ , and  $\kappa_{Z\gamma}$  to account for potential BSM contributions.

### 1. Model-I

In the first model, couplings are simplified to two scale factors:  $\kappa_V = \kappa_W = \kappa_Z$  for vector bosons and  $\kappa_F$  for all fermions. No invisible or undetected decays beyond the SM are assumed ( $B_{\text{inv.}} = B_u = 0$ ), and only the relative sign between  $\kappa_V$  and  $\kappa_F$  is physical, with  $\kappa_V, \kappa_F \geq 0$ . A combined fit yields  $\kappa_V = 1.035 \pm 0.031$ ,  $\kappa_F = 0.95 \pm 0.05$ , consistent with the SM, and shows a 39% positive correlation between the two parameters. The relatively large positive correlation of 39% is observed between the two fit parameters, since some of the most sensitive input measurements involve the ggF production process (i.e. via couplings to fermions) with subsequent Higgs boson decays into vector bosons. Figure 35 shows the combined fit results in a  $(\kappa_V, \kappa_F)$  plane.

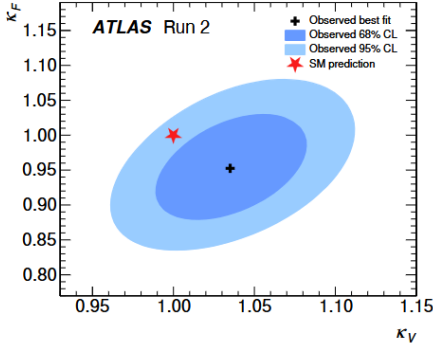


FIG. 35: Negative log-likelihood contours corresponding to 68% and 95% CL in the  $(\kappa_V, \kappa_F)$  plane. They are obtained from a combined fit assuming no contributions from invisible or undetected non-SM Higgs boson decays. The  $p$ -value for compatibility of the combined measurement and the SM prediction is 14%.

### 2. Model-II

In the second class of models, the coupling strength modifiers  $\kappa_W$ ,  $\kappa_Z$ ,  $\kappa_t$ ,  $\kappa_b$ ,  $\kappa_c$ ,  $\kappa_\tau$ , and  $\kappa_\mu$  are treated as independent, positive parameters. It is assumed that

only Standard Model (SM) particles contribute to loop-induced processes, with modifications to fermion and vector boson couplings propagated accordingly. Invisible or undetected non-SM Higgs decays are not considered.

These models enable a test of the predicted mass scaling of the Higgs couplings using reduced coupling strength modifiers:

$$\sqrt{\frac{\kappa_v g_v}{2 \text{ vev}}} = \sqrt{\kappa_v} \frac{m_v}{\text{vev}}, \quad (67)$$

$$\kappa_F g_F = \frac{\kappa_F m_F}{\text{vev}}, \quad (68)$$

where  $g_v$  and  $g_F$  are the coupling strengths for vector bosons and fermions, respectively;  $m_V$  and  $m_F$  are the masses of the weak bosons and fermions, respectively, and  $\text{vev}$  is the vacuum expectation value of the Higgs field. The structure of  $\kappa$  comes directly from the form of the relevant Yukawa coupling involved.

Figure 36 presents results for two scenarios: (i) with the charm quark coupling constrained by  $\kappa_c = \kappa_t$ , and (ii) with  $\kappa_c$  as a free parameter. In both cases, the measured coupling strength modifiers are found to be consistent with SM predictions.

When  $\kappa_c$  is unconstrained, an observed (expected) upper limit of  $\kappa_c < 5.7$  (7.6) times the SM prediction is obtained at 95% confidence level (CL), improving upon the previous limit of  $\kappa_c < 8.5$  (12.4) from the  $H \rightarrow c\bar{c}$  decay measurement[20]. This improvement arises despite relaxed assumptions, due to global constraints on the total Higgs width, which affect all coupling measurements.

### 3. Model-III

The third class of models in the  $\kappa$ -framework builds upon the previous one by allowing non-SM particles to contribute to loop-induced processes. These processes are parametrized using effective coupling strength modifiers  $\kappa_g$ ,  $\kappa_\gamma$ , and  $\kappa_{Z\gamma}$ , through loop calculations, instead of modified SM couplings. We assume BSM<sup>15</sup> effects do not significantly alter the kinematics of Higgs decay products.

Two scenarios are considered: one where invisible or undetected non-SM Higgs decays are not allowed ( $B_{\text{inv.}} = B_u = 0$ ), and another where such decays are permitted (Figure 37 shows both scenarios). In the latter case, constraints are imposed to avoid degeneracies:  $B_u \geq 0$  and  $\kappa_V \leq 1$ . These constraints generally turn up from BSM considerations.

Again, measured  $\kappa$  are found to be compatible with SM expectations. When non-SM decays are allowed, the fitted values of previously measured couplings remain mostly unchanged. However, upper limits are set at 95% CL:

<sup>15</sup> Beyond the Standard Model

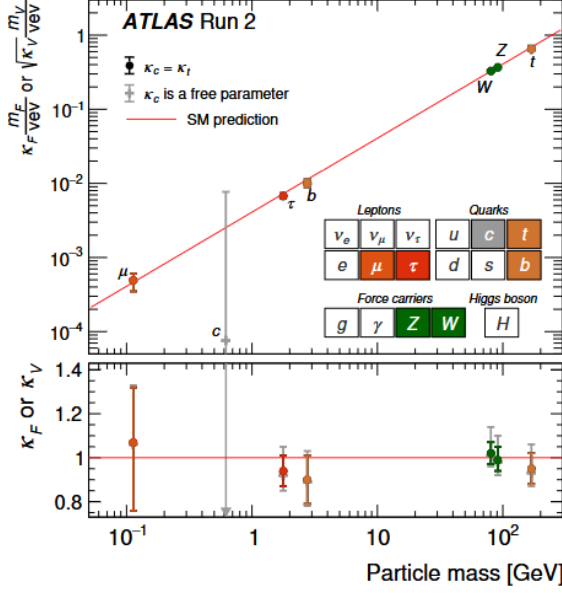


FIG. 36: Reduced Higgs boson coupling strength modifiers and their uncertainties. Two fit scenarios with  $\kappa_c = \kappa_t$  (coloured circle markers), or  $\kappa_c$  left free-floating in the fit (grey cross markers) are shown. Loop-induced processes are assumed to have the SM structure, and Higgs boson decays to non-SM particles are not allowed.

The vertical bar on each point denotes the 68% confidence interval. The  $p$ -values for compatibility of the combined measurement and the SM prediction are 56% and 65% for the respective scenarios. The lower panel shows the values of the coupling strength modifiers. The grey arrow points in the direction of the best-fit value and the corresponding grey uncertainty bar extends beyond the lower panel range

- $B_u < 0.12$  (expected 0.21),
- $B_{\text{inv.}} < 0.13$  (expected 0.08),

improving upon the best existing limit of  $B_{\text{inv.}} < 0.145$  (expected 0.103) from direct ATLAS searches[21].

#### D. Higgs Mass and Lifetime

Understanding the properties of the SM-like Higgs boson and the symmetry structure of the Higgs Lagrangian is the first task when we want to interpret LHC Higgs measurements in terms of a QFT. Its discovery in 2012 at LHC confirmed the mechanism of electroweak symmetry breaking, which gives mass to other particles.

To fully understand the physics behind the Higgs Boson, we study:

- The Higgs mass (which was the last unknown SM parameter before discovery). Although SM predicted the existence of the Higgs, it did not predict

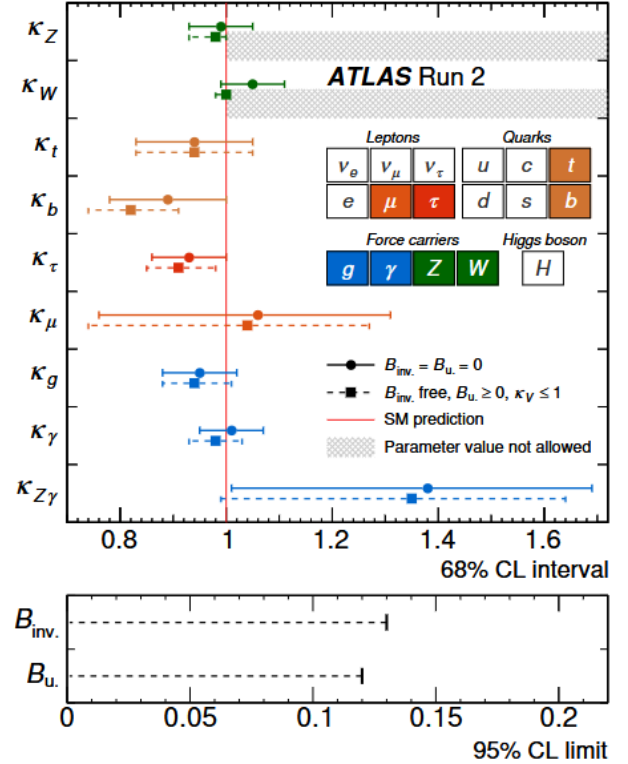


FIG. 37: Reduced coupling strength modifiers and their uncertainties per particle type with effective photon,  $Z\gamma$  and gluon couplings. The horizontal bars on each point represent the 68% confidence intervals. The scenario assuming  $B_{\text{inv.}} = B_u = 0$  is shown using solid lines with circular markers. In this case, the  $p$ -value for compatibility with the SM prediction is 61%. The alternative scenario, where  $B_{\text{inv.}}$  and  $B_u$  are allowed to contribute to the total Higgs boson decay width under the assumptions  $\kappa_V \leq 1$  and  $B_u \geq 0$ , is shown using dashed lines with square markers. The lower panel displays the 95% CL upper limits on  $B_{\text{inv.}}$  and  $B_u$ .

its exact mass. However, indirect constraints from electroweak precision data suggested it should be light ( $<140$  GeV).

- The Higgs decay width and lifetime (related to its stability and possible BSM physics).
- How properties of the Higgs affect electroweak precision tests and the validity of SM.

We have already discussed theoretical constraints on the Higgs mass and relevant theoretical decay rates in Section II. We still do quick review of relevant results and then move on to CP-related properties of the Higgs boson.

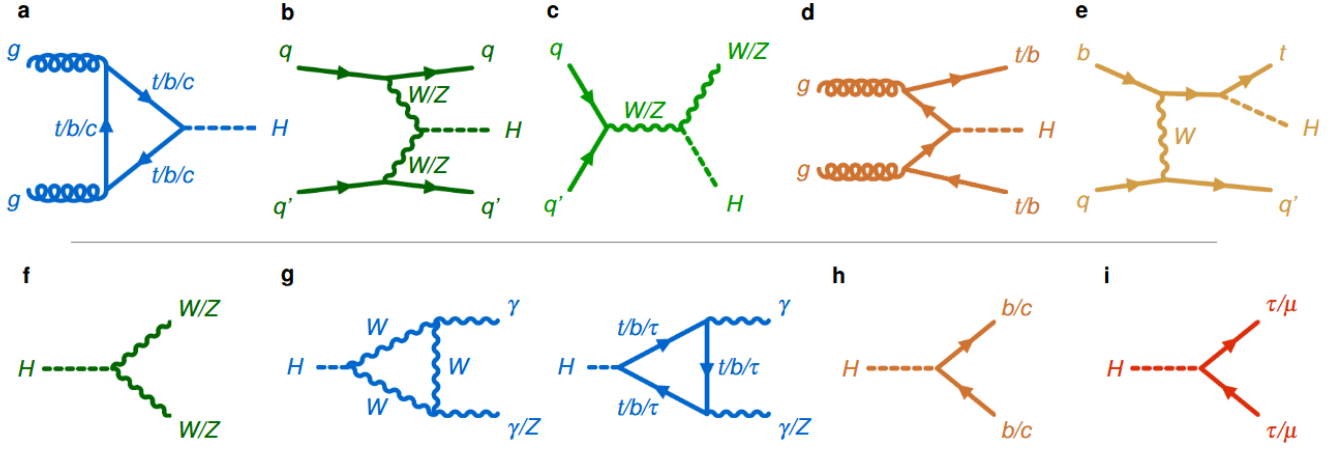


FIG. 38: Examples of Feynman diagrams for Higgs boson production and decays. The Higgs boson is produced via gluon–gluon fusion (a), vector-boson fusion (VBF; b), and associated production with vector bosons (c), top- or  $b$ -quark pairs (d), or a single top quark (e). f–i, The Higgs boson decays into a pair of vector bosons (f), a pair of photons or a  $Z$  boson and a photon (g), a pair of quarks (h), and a pair of charged leptons (i). Loop-induced Higgs boson interactions with gluons or photons are shown in blue, processes involving couplings to  $W$  or  $Z$  bosons in green, to quarks in orange, and to leptons in red. Two different shades of green (orange) are used to separate the VBF and  $VH$  ( $ttH$  and  $tH$ ) production processes.

### 1. Theoretical Constraints on the Higgs Mass

Electroweak symmetry breaking requires the Higgs mass to be within a range where SM calculations remain valid (perturbative regime). If the Higgs were too heavy (near the  $WW$  threshold, which is  $\sim 160$  GeV), higher-order quantum corrections would destabilize predictions. Custodial symmetry (a property of the Higgs mechanism) also imposes constraints; the Higgs mass affects the isospin violation parameter or  $T$ -parameter, which must remain small.

### 2. Higgs Decay Width and Lifetime

If the width is larger than predicted by the SM, it could imply:

- New decay channels (like the Higgs decaying to invisible dark matter).
- Exotic interactions beyond the SM.

If the width is smaller, it would imply suppressed couplings or new physics effects. The width  $\Gamma_K$  measures how quickly Higgs decays. In the SM, for  $M_h \sim 125$  GeV, the predicted width is:

$$\Gamma_h \sim 4 \text{ MeV} \quad (69)$$

This is extremely narrow compared to the detector resolution ( $\sim 1$  GeV), making direct measurements difficult.

### 3. Challenges in Measuring the Width

LHC cannot directly measure  $\Gamma_h$  due to limited detector resolution. Instead, indirect methods are used, such as:

- Interference effects (e.g.,  $gg \rightarrow H \rightarrow ZZ$  vs  $gg \rightarrow ZZ$  background).
- Off-shell vs on-shell Higgs production.

Future colliders like FCC, ILC may achieve better precision. We will come back to this issue in a later section.

*a. Extracting the Higgs Width from Off-Shell Production* Since the Higgs width is too small ( $\sim 4$  MeV) to measure directly at the LHC, physicists use an indirect method. Comparing on-shell ( $M_h \sim 125$  GeV) and off-shell ( $M_{4l} > 140$  GeV) Higgs production in the process:

$$gg \rightarrow ZZ^* \rightarrow 4l \quad (70)$$

The Higgs propagator in the amplitude is given by:

$$\Gamma = \frac{1}{(m_{4l}^2 - M_h^2)^2 + M_h^2 \Gamma_h^2} \quad (71)$$

By measuring the  $gg \rightarrow 4l$  rate above and on the resonance, we can extract information about the Higgs width.

ATLAS and CMS have used this technique to place limits on the Higgs width:

$$\Gamma_h < (4 - 5) \Gamma_h^{SM} \quad (72)$$

#### 4. Challenges and Assumptions

The Higgs coupling to gluons is loop-induced and can have a non-trivial dependence on all masses involved. Thus, extracting the Higgs width requires assuming that:

- All interactions are those of the SM.
- No exotic decays or new physics contributions exist.

#### 5. Future Improvements

- High Luminosity LHC (HL-LHC): more data will reduce uncertainties.
- Future lepton colliders (FCC-ee, ILC) could measure the width directly via Higgsstrahlung with better precision.

### E. Spin

After the Higgs discovery, a critical question was: does it have spin zero (as predicted by SM)? Alternative possibilities (spin 1 and spin 2) had to be ruled out.

#### 1. Theoretical Framework: EFT Approach

Since no visible renormalizable theories predict alternative Higgs spin, physicists used an effective Lagrangian

$$\begin{aligned}
 L^{j=1} = & i g_1^{(1)} (W_{\mu\nu}^+ W^{-\mu} - W_{\mu\nu}^- W^{+\mu}) Y^{(e)\nu} + i g_2^{(1)} W_\mu^+ W_\nu^- Y^{(e)\mu\nu} + g_3^{(1)} \epsilon^{\mu\nu\rho\sigma} (W_\mu^+ \overleftrightarrow{\partial}_\rho W_\nu^-) Y_\sigma^{(e)} \\
 & + i g_4^{(1)} \tilde{W}_{\sigma\mu}^+ W^{-\mu\nu} Y_\nu^{(e)\sigma} - g_5^{(1)} W_\mu^+ W_\nu^- (\partial^\mu Y^{(o)\nu} + \partial^\nu Y^{(o)\mu}) + i g_6^{(1)} W_\mu^+ W_\nu^- \tilde{Y}^{(o)\mu\nu} \\
 & + i g_7^{(1)} \tilde{W}_{\sigma\mu}^+ W^{-\mu\nu} \tilde{Y}_\nu^{(o)\sigma} + g_8^{(1)} \epsilon^{\mu\nu\rho\sigma} Y_\mu^{(e)} Z_\nu (\partial_\rho Z_\sigma) + g_9^{(1)} Y_\mu^{(o)} (\partial_\nu Z^\mu) Z^\nu
 \end{aligned} \quad (74)$$

- **Spin-2 (Tensor particle):** Couples via the energy-momentum tensor (Equation 75).

$$L^{j=2} = -g_1^{(2)} G^{\mu\nu} T_{\mu\nu V} - g_2^{(2)} G^{\mu\nu} T_{\mu\nu G} - g_3^{(2)} G^{\mu\nu} T_{\mu\nu f} \quad (75)$$

#### 3. Experimental Tests and Results

*a. Spin-0 vs Spin-2 Discrimination* ATLAS and CMS compared  $h \rightarrow ZZ^* \rightarrow 4l$  angular distributions, where spin-2 predicts a different  $\cos\theta^*$  dependence than spin-0. Data strongly favors spin-0 (Fig. 2, right).

*b. CP Even vs CP Odd Tests* A pseudoscalar Higgs, which is CP-odd, would have different  $h \rightarrow \tau\tau$  decay distributions. Moreover, opposite  $h \rightarrow \gamma\gamma$  polarization

to test different spin/CP hypotheses.

The effective interactions that were used to constrain such couplings or to contrast with the SM Higgs in simple hypothesis tests need to be understood as straw-man proposals. They are not motivated by the actual models and they typically cannot be understood in terms of renormalizable theories.

#### 2. Possible Spin Hypotheses

- **Spin-0 (scalar/pseudoscalar):** CP-even (scalar, like SM Higgs) (Equation 73)

$$\begin{aligned}
 L^{j=0} = & g_1^{(0)} h V^\mu V_\mu - \frac{g_2^{(0)}}{4} h V^{\mu\nu} V_{\mu\nu} - \frac{g_3^{(0)}}{4} A V^{\mu\nu} \widetilde{V}_{\mu\nu} \\
 & - \frac{g_4^{(0)}}{4} h G^{\mu\nu} G_{\mu\nu} - \frac{g_5^{(0)}}{4} A G^{\mu\nu} \widetilde{G}_{\mu\nu}
 \end{aligned} \quad (73)$$

- **Spin-1 (Vector boson):** Ruled out early because spin-1 (Equation 74) predicts different angular correlations  $H \rightarrow \gamma\gamma$  and  $H \rightarrow ZZ$ .

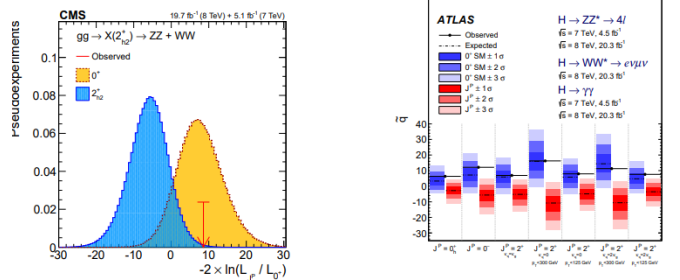


FIG. 39: Left: comparison of CP-even vs. CP-odd scalar hypotheses. Right: comparisons of various alternate hypotheses against the SM Higgs boson

effects could arise. However, experimental findings indicate that the Higgs is mostly CP-even, but small CP-odd admixtures are still allowed (10-20%).

*c. Spin-1 Exclusion* Spin-1 predicts forbidden decay modes, for example,  $H \rightarrow \gamma Z$ , which can vanish in spin-0 but not in spin-1. LHC data excludes pure spin-1 at greater than 99.9% confidence level.

## F. Constraining Higgs Spin and CP Properties Using Angular Distributions and Cross-Section Analysis

After the Higgs boson discovery, a crucial task was to verify its spin and CP properties by studying its decay angular distributions. This is done by analyzing the kinematics of decays like  $X \rightarrow WW, ZZ$  where  $X$  is the Higgs or an imposter.

To distinguish between different spin/CP hypotheses, we define reference frames and angles (Figure 40). Now, let us define the kinematic variables:

$$\cos \theta_h = \frac{\tilde{p}_\alpha \cdot \tilde{p}_X}{\sqrt{\tilde{p}_\alpha^2 \tilde{p}_X^2}}|_{Z_h}, \quad \cos \theta_l = \frac{\tilde{p}_- \cdot \tilde{p}_X}{\sqrt{\tilde{p}_-^2 \tilde{p}_X^2}}|_{Z_l}, \quad \cos \theta^* = \frac{\tilde{p}_{Z_l} \cdot \hat{e}_z}{\sqrt{\tilde{p}_{Z_l}^2}}|_X \quad (76)$$

$$\cos \Phi_1 = \frac{(\hat{e}_z \times \hat{e}_z^0) \cdot (\tilde{p}_\alpha \times \tilde{p}_\beta)}{\sqrt{(\tilde{p}_\alpha \times \tilde{p}_\beta)^2}}|_X, \quad \cos \Phi = \frac{(\tilde{p}_\alpha \times \tilde{p}_\beta) \cdot (\tilde{p}_- \times \tilde{p}_+)}{\sqrt{(\tilde{p}_\alpha \times \tilde{p}_\beta)^2 (\tilde{p}_- \times \tilde{p}_+)^2}}|_X \quad (77)$$

Spin-0 Higgs bosons produce specific angular distributions; for example,  $\cos \theta^*$  peaks at 0 and  $\pi$ . Spin-1 and spin-2 bosons yield different distributions from this distribution and acts as a discriminator, as seen in .

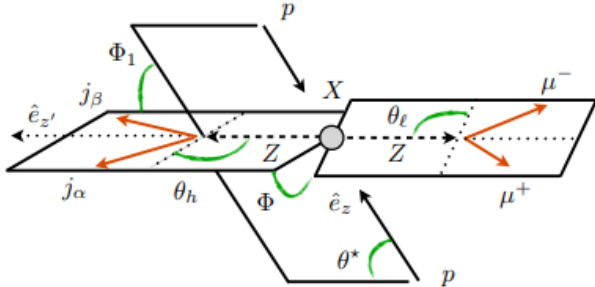


FIG. 40: Angles sensitive to the spin and CP characterization program

## 1. Momentum Definitions in the Higgs Rest Frame

$$\begin{aligned} \vec{p}_{Zh} &= \vec{p}_\alpha + \vec{p}_\beta \quad (\text{Z from h decay}) \\ \vec{p}_{Zl} &= \vec{p}_+ + \vec{p}_- \quad (\text{Z leptonic decay}) \\ \vec{p}_X &= \vec{p}_{Zh} + \vec{p}_{Zl} \quad (\text{Total Higgs Momentum}) \end{aligned}$$

## 2. Angular Definitions

- $\cos \theta_h$  is the angle between  $\vec{p}_\alpha$  (from  $Z \rightarrow \ell\ell$ ) and  $\vec{p}_X$  (Higgs direction).
- $\cos \theta_l$  is the angle between  $\vec{p}_-$  (lepton) and  $\vec{p}_X$ .
- The Collins-Soper angle ( $\cos \theta^*$ ) is the angle between the beam axis and the  $ZZ$  decay axis in the Higgs frame.
- The azimuthal angle  $\cos \Phi_1$  correlates the  $Z$  decay plane orientation with the beam axis.
- $\cos \Phi$  relates the two  $Z$  decay planes.

The analytical expressions are given by:

ATLAS and CMS performed template fits comparing data to different spin/CP hypotheses. An example is shown in Figure 39, which ruled out non-spin 0 hypotheses.

## G. CP Properties

The three discrete symmetries consistent with Lorentz invariance and a Hermitian Hamiltonian are charge conjugation (C), parity (P), and time reversal (T). Their actions are defined as follows:

### 1. Symmetry Transformations

- **Charge Conjugation (C):** For a scalar field  $\phi(t, X)$ ,

$$C\phi(t, X)C^{-1} = \eta_c \phi^*(t, X) \quad (78)$$

where  $\phi^*$  is the complex conjugate of the scalar field, and  $\eta_c$  is a phase factor.

- **Parity (P):**

$$P\phi(t, X)P^{-1} = \eta_p\phi(t, -X) \quad (79)$$

where  $\eta_p$  is the intrinsic parity of the field.

- **Time Reversal (T):**

$$T\phi(t, X)T^{-1} = \phi(-t, X) \quad (80)$$

### 2. Transforming to Momentum-Spin Space

In terms of momentum ( $\vec{p}$ ) and spin ( $\vec{s}$ ), the transformations take the form:

$$C : C|\phi(p, s)\rangle = |\phi^*(p, s)\rangle \quad (\text{particle} \leftrightarrow \text{antiparticle})$$

$$P : P|\phi(p, s)\rangle = \eta_p|\phi(-p, s)\rangle \quad (\text{flips momentum, keeps spin})$$

$$T : T|\phi(p, s)\rangle = |\phi(-p, -s)\rangle$$

### 3. Observables and Symmetry Tests

An observable is a measurable quantity like momentum and spin. Observables can be classified based on their behavior under C, P, and T:

- **U-even observable:**  $O(U|i\rangle \rightarrow U|f\rangle) = +O(|i\rangle \rightarrow |f\rangle)$  (remains unchanged).
- **U-odd observable:**  $O(U|i\rangle \rightarrow U|f\rangle) = -O(|i\rangle \rightarrow |f\rangle)$  (changes sign).

If the underlying physics respects U symmetry, the average of a genuine U-odd observable is zero. This helps test symmetry violation.

For LHC analysis, CP transformation properties relate to T transformation. If CP is conserved, the expectation value of a T-odd observable is zero, whereas a nonzero value indicates CP violation.

### 4. CP Tests at Hadron Colliders

At the LHC, collisions of quarks and gluons produce particles, but we cannot measure their spins or charges directly. Instead, we analyze their momenta. Scalar products of momenta help define CP observables.

Using the Levi-Civita tensor, we construct a unique P-odd and T-odd observable to test CP violation. Higgs processes define three CP-odd observables: two CP-odd, T-even (from scalar products) and one CP-odd, T-odd (from Levi-Civita construction).

- **Case 1: CP-odd and T-odd:** If CP is conserved,  $\langle O \rangle = 0$ . If violated,  $\langle O \rangle \neq 0$  (independent of rescattering).

- **CP-Odd and T-Even Observables** If CP is conserved, we expect  $\langle O \rangle = 0$ . However, if CP is violated,  $\langle O \rangle \neq 0$  only if rescattering (final-state interactions) is present. Without rescattering, T symmetry forces  $\langle O \rangle = 0$  even if CP is violated. This means that CP-odd and T-even observables require rescattering effects to reveal CP violation.

T-odd observables provide a cleaner probe for CP violation since they do not require rescattering to yield a nonzero measurement.

Here are some Feynman diagrams describing three processes useful for analyzing Higgs CP properties: WBF Higgs production, associated Zh production and  $h \rightarrow 4\ell$  decays respectively.

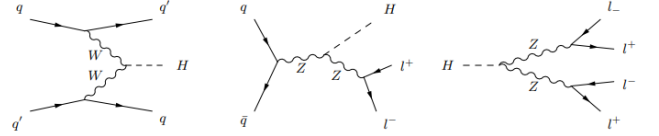


FIG. 41: : Feynman diagrams describing three processes useful for analyzing Higgs CP properties: WBF Higgs production, associated Zh production, and  $H \rightarrow 4\ell$  decays.

### 5. Studying Higgs Symmetries (C, P, T) at the LHC

Scientists at the Large Hadron Collider (LHC) study how the Higgs boson interacts with other particles by analyzing symmetries (C = charge, P = parity, T = time). Two main interactions are studied:

1. Higgs-fermion interactions (e.g., with top quarks or tau leptons).
2. Higgs-gauge boson interactions (e.g., with W/Z bosons).

### 6. Higgs-Fermion Interactions (CP Violation)

Normally, the Higgs-fermion interaction is CP-even (symmetric under charge-parity). But we can add a CP-odd term:

**Original CP-even Lagrangian :**

$$-y_u \bar{Q}_L \tilde{\phi} u_R \quad (81)$$

**Modified Lagrangian with CP-odd term :**

$$-y_u \bar{Q}_L \tilde{\phi} (c_\alpha 1 + i s_\alpha \gamma_5) u_R \quad (82)$$

where:

- $c_\alpha = \cos \alpha$ ,  $s_\alpha = \sin \alpha$  (mixing angle).



Observable	Theory	Re-scattering	Prediction
CP-odd, T-odd	CP-symmetric	no	$\sigma_{\text{int}}$ symmetric, odd $O \Rightarrow \langle O \rangle = 0$
		yes	$\sigma_{\text{int}}$ symmetric, odd $O \Rightarrow \langle O \rangle = 0$
	CP-violating	no	Can have $\langle O \rangle \neq 0$
		yes	Can have $\langle O \rangle \neq 0$
CP-odd, T-even	CP-symmetric	no	$\sigma_{\text{int}}$ symmetric, odd $O \Rightarrow \langle O \rangle = 0$
		yes	$\sigma_{\text{int}}$ symmetric, odd $O \Rightarrow \langle O \rangle = 0$
	CP-violating	no	$\sigma_{\text{int}}$ anti-symmetric, even $O \Rightarrow \langle O \rangle = 0$
		yes	Can have $\langle O \rangle \neq 0$

TABLE III: Predictions for CP-odd observables  $O$  based on the theory's symmetries and the observable's transformation properties under  $\hat{T}$ . We assume the initial state or its probability distribution is symmetric under both CP and  $\hat{T}$ .

- $\gamma_5$  introduces parity (P) and CP violation.
- The size of the Yukawa coupling must match observed Higgs production rates.

### How can we detect CP violation?

- For top quarks: Measure the angle between decay leptons in boosted events.
- For tau leptons: Use  $\tau\tau$  polarization in  $H \rightarrow \tau^+\tau^-$ .

#### 7. Higgs-Gauge Interactions (CP Violation at Dimension-6)

For Higgs interactions with gauge bosons (W, Z, photons), CP violation only appears in higher-order terms (dimension-6 operators).

##### CP-odd operators:

$$O_{B\tilde{B}} = -\frac{g_0^2}{4}(\phi^\dagger\phi)\widetilde{B^{\mu\nu}}B_{\mu\nu} \equiv -\frac{g_0^2}{4}(\phi^\dagger\phi)\epsilon^{\mu\nu\rho\sigma}B_{\rho\sigma}B_{\mu\nu} \quad (83)$$

$$O_{W\tilde{W}} = -\frac{g^2}{4}(\phi^\dagger\phi)W^{k\mu\nu}\widetilde{W_{\mu\nu}^k} \equiv -\frac{g^2}{4}(\phi^\dagger\phi)\epsilon_{\mu\nu\rho\sigma}W^{k\rho\sigma}W^{k\mu\nu} \quad (84)$$

With the Levi-Civita tensor, these operators are C-conserving, P-violating, and CP-violating. The hard process which will allow us to determine the CP-properties of the gauge-Higgs interactions needs to include the  $WWh$  or  $ZZh$  coupling. As illustrated in Figure 41, this points to WBF Higgs production, associated  $Vh$  production, or  $h \rightarrow 4l$  decays. The leading observable to test CP-violation is the one P-odd and  $\hat{T}$ -odd observable constructed with the help of the Levi-Civita tensor. For the three different hard processes, it corresponds to the signed azimuthal angle between the WBF tagging jets, the azimuthal angle between the leptons from the Z-decay, or the decay plane correlations in the Higgs decays. In the right panel of Figure 42, we show the distribution of the signed azimuthal angle between the WBF tagging jets for different Wilson coefficients defined in the above equation. The interference with the SM rate is

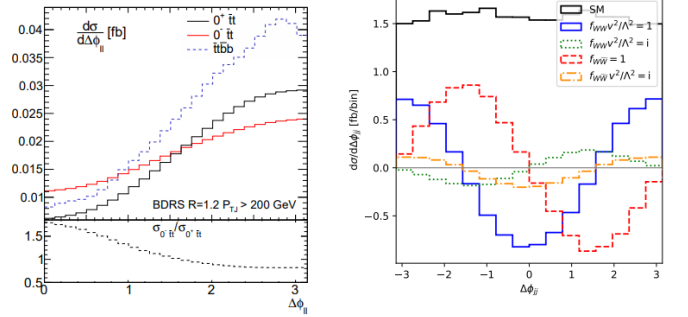


FIG. 42: Left: Azimuthal angle between the top decay leptons for  $ttth$  production for CP-even and CP-odd couplings, figure from Ref. [22]. Right: Signed azimuthal angle between the tagging jets in WBF Higgs production for CP-even and CP-odd couplings with real and (hypothetically) imaginary Wilson coefficients, figure from Ref. [23]

indeed anti-symmetric for the CP-odd coupling. Imaginary Wilson-like coefficients are not part of a consistent EFT prescription, but they can be used to illustrate the effect of re-scattering.

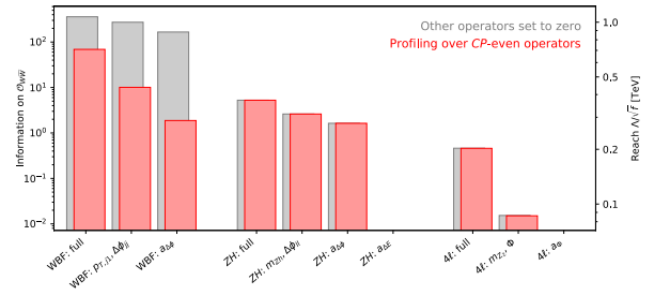


FIG. 43: Comparison of WBF Higgs production,  $Zh$  production, and  $h \rightarrow 4l$  decays, in terms of their reach for CP-violating Higgs couplings. The reach is defined in terms of the effective interaction  $f/\Lambda^2 O_{W\tilde{W}}$  defined in Equation 84. The reach is computed by matching order one new physics effects at new physics scale  $\Lambda$ :  $1/\Lambda^2 = f/\Lambda^2$

When we use appropriate kinematic distributions to search for effects from the specific CP-odd operators of the above equation, the performance of angular correlations can be enhanced by including momenta in the CP-observables. The reason is that the dimension-6 operators have a new Lorentz structure, which comes with powers of 4-momenta in the Feynman rules. In Figure 43, we show a comparison of the reach of the three leading signatures for CP-violation in the Higgs-gauge sector. The corresponding Feynman diagrams are shown in Figure 41. The reach in terms of the new physics scale  $\Lambda$  is shown on the right axis; it is computed using the Fisher information and information geometry. For each channel, we compute the information available from the full phase space after basic acceptance cuts, from a combination of momentum-sensitive and CP-sensitive observables, and from the (optimal) CP-sensitive observable. For WBF Higgs production, the latter is defined as an asymmetry in the signed azimuthal angle between the tagging jets,

$$a_{\Delta\Phi_{jj}} = \frac{d\sigma(\Delta\phi_{jj}) - d\sigma(-\Delta\phi_{jj})}{d\sigma(\Delta\phi_{jj}) + d\sigma(-\Delta\phi_{jj})}. \quad (85)$$

For the other two channels, we use the appropriate combination of final state momenta instead. While WBF Higgs production and  $Zh$  production indicate a similar reach, the Higgs decay channels are clearly less powerful.

Once we have convinced ourselves through these dedicated measurements that CP is not a good symmetry of the gauge-Higgs sector, the operators need to be included in global Higgs analysis.

## V. LATEST DEVELOPMENTS AND FUTURE OUTLOOKS

We now delve into some current experimental advances in Higgs-based measurements. An important factor common to all these developments, in addition to pure hardware upgrades and greater data collection is the inclusion of more optimized machine learning methods in order to classify signals in our experiments.

### A. ATLAS Run-3 Assets

On 5 July 2022, after over 3 years of shutdown, the LHC returned with a new energy world record of 13.6 trillion electron volts (13.6 TeV) in its first stable-beam collisions. These collisions mark the start of data-taking for the new physics season, called Run 3.

Run-3 is accompanied by an increase in the precision of measurements through the inclusion of an increase in total data available, as well as more final states. An important development is *data parking*, also known as *delayed reconstruction*, which allows ATLAS systems to take more data than can be processed instantaneously. This ‘parked data’ can later be processed when CPUs

are available, for example, during shutdown periods of the LHC.

*Trigger level analysis* or *data scouting*, is another new technique to optimise data processing. As we saw earlier, (during the search for the Higgs), various triggers must be activated for signals to register. However, due to excess total events occurring, all events may not be recorded. In TLA, some of these trigger conditions are relaxed and all events satisfying less stringent criteria are recorded. This allows for simpler data analysis, and ends up allowing us to save larger volume of data for post-processing.

Finally, there are newer detectors being employed, like the *Muon New Small Wheel* which increases efficiency of the end-cap region of the ATLAS detector, described earlier. A new Liquid Argon Calorimeter, along with digital triggering provides higher granularity and resolution for better feature extraction.[24]

### B. Transformer-Based Measurements of $t\bar{t}H$

Recent Run-2 measurements of the associated production of a Higgs boson with a top-quark pair was measured in the  $H \rightarrow b\bar{b}$  decay ( $t\bar{t}H(bb)$ ) mode have demonstrated a significant increase in signal significance, primarily due to advances in classification methods and improved  $b$ -jet identification using artificial neural networks. These developments have also led to better separation from background processes.

In the study[25],  $t\bar{t}H(bb)$  was analyzed using 140 fb $^{-1}$  of  $\sqrt{s} = 13$  TeV  $pp$  collision data collected by the ATLAS detector. Final states with one or two leptons were analyzed. Assuming  $m_H = 125.09$  GeV, the measured inclusive cross-section was found to be:

$$\sigma(t\bar{t}H) = 411 \pm 54 \text{ (stat.)}_{-75}^{+85} \text{ (syst.) fb,}$$

with a 24% total uncertainty, consistent with Standard Model predictions. The dominant uncertainties arise from  $t\bar{t}H$  signal modelling and  $t\bar{t}$  + jets background. The observed (expected) significance is 4.6 (5.4) standard deviations (see Figure 45).

Compared to previous analyses, this result benefits from improved  $b$ -jet identification and looser selection criteria, enhancing signal acceptance. A multiclass neural network is used to define control regions enriched in  $t\bar{t}$  + jets components. Dedicated modeling for  $t\bar{t} + \geq 1b$  and data-driven corrections for  $t\bar{t} + \geq 1c$  and light-flavor jets significantly reduce background modelling uncertainties. This measurement is the most precise  $t\bar{t}H$  cross-section determination in a single decay channel, both inclusively and differentially in  $p_T^H$ .

The essential idea involved in this method was using a neural network to correct expected signal yields through input (measured) data, which allowed both signal and background yields to be corrected (In Figure 45, S and B are these corrected yields). These currents allowed lesser uncertainty and higher precision in the  $\sigma(t\bar{t}H)$  value obtained.



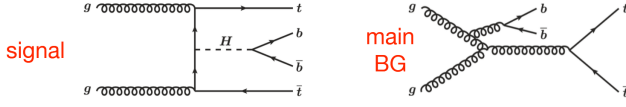


FIG. 44: Improvements in signal classification and  $b$ -tagging for  $ttH$  analysis.<sup>a</sup>

<sup>a</sup> Adapted from Giagu S., ATLAS Collaboration, BCVSPIN2024.

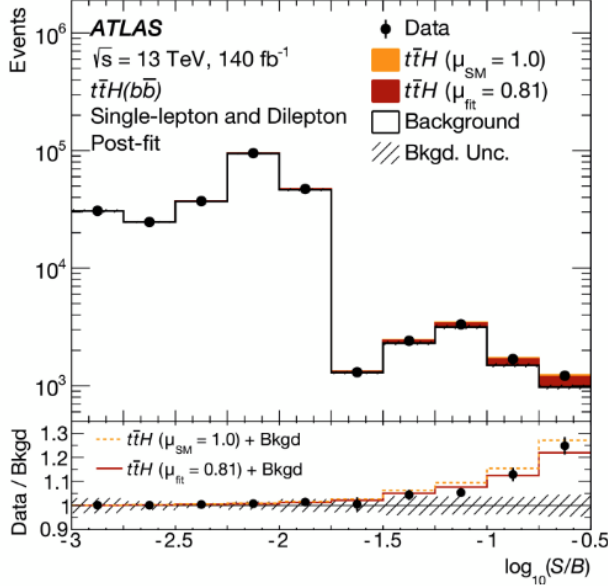


FIG. 45: Observed and expected event yields as a function of  $\log_{10}(S/B)$  where  $S$  and  $B$  are the post-fit signal and total background yields, respectively. The bins in all fitted regions are ordered and grouped in bins of  $\log_{10}(S/B)$ . The signal is shown for the best-fit signal strength,  $\mu = 0.81$ , or the SM prediction,  $\mu_{SM} = 1.0$ . The lower panel shows the ratio of the data to the post-fit background prediction, compared with the signal-plus-background prediction with the best-fit signal strength and the SM prediction. The shaded band represents the total uncertainty in the background prediction.

### C. Off-Shell Higgs Production from $ZZ$ Leptonic Decays

Off-shell Higgs production in the  $gg \rightarrow H^* \rightarrow ZZ$  channel can be used to probe Higgs properties beyond the narrow width approximation. The on-shell and off-shell cross-sections differ in their dependence on the total Higgs width  $\Gamma_H$ :

$$\sigma_{gg \rightarrow H \rightarrow ZZ}^{\text{on-shell}} \sim \frac{g_{ggF}^2 g_{HZZ}^2}{m_H \Gamma_H} \quad (86)$$

$$\sigma_{gg \rightarrow H \rightarrow ZZ}^{\text{off-shell}} \sim \frac{g_{ggF}^2 g_{HZZ}^2}{m_{ZZ}^2} \quad (87)$$

We may do a rough calculation to see how these expressions arise.

#### 1. Dependence of $\sigma$ on off-shell $v/s$ on-shell measurements

The Higgs boson mediates the process  $gg \rightarrow H \rightarrow ZZ$  as a resonance. The total cross-section is proportional to the square of the propagator and the relevant couplings.

*a. On-shell production* When the invariant mass of the final state satisfies  $m_{ZZ} \approx m_H$ , the Higgs boson is produced on-shell and the propagator follows the Breit-Wigner form:

$$\left| \frac{1}{s - m_H^2 + im_H \Gamma_H} \right|^2 \approx \frac{1}{(m_H \Gamma_H)^2}$$

Thus, the on-shell cross-section behaves as:

$$\sigma_{gg \rightarrow H \rightarrow ZZ}^{\text{on-shell}} \sim \frac{g_{ggF}^2 \cdot g_{HZZ}^2}{m_H \Gamma_H}$$

where:

- $g_{ggF}$ : effective coupling of the Higgs to gluons,
- $g_{HZZ}$ : coupling of the Higgs to  $ZZ$ ,
- $\Gamma_H$ : total Higgs width.

*b. Off-shell production* In the off-shell regime, where  $m_{ZZ} \gg m_H$ , the imaginary part of the propagator becomes negligible, and:

$$\left| \frac{1}{s - m_H^2 + im_H \Gamma_H} \right|^2 \approx \frac{1}{(s - m_H^2)^2} \sim \frac{1}{m_{ZZ}^4}$$

However, the phase space grows with  $m_{ZZ}^2$ , yielding:

$$\sigma_{gg \rightarrow H \rightarrow ZZ}^{\text{off-shell}} \sim \frac{g_{ggF}^2 \cdot g_{HZZ}^2}{m_{ZZ}^2}$$

Off-shell production becomes increasingly accessible as the phase space for  $ZZ$  decays opens up at higher invariant masses.

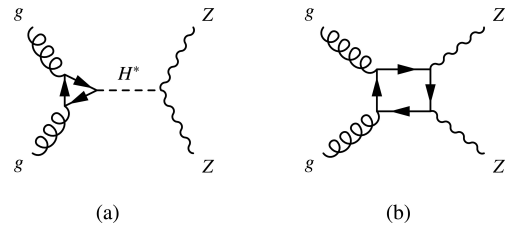


FIG. 46: Leading-order Feynman diagrams for (a) signal  $gg \rightarrow H^* \rightarrow ZZ$  and (b) background processes.

The particle technique which allows more precise inferences from measured data is known as *Neural Simulation-Based Inference (NSBI)*. NSBI provides a

machine learning-based approximation to full matrix elements at the detector level, achieving up to 20% better sensitivity in off-shell Higgs searches.[26]

On combining with  $H \rightarrow ZZ^* \rightarrow 2\ell 2\nu$ , measurements and analyses done using NSBI excludes the hypothesis of no off-shell Higgs boson production with an observed significance of  $3.7\sigma$  (expected  $2.4\sigma$ ). This was the first piece of evidence of off-shell production in Run-2 data provided by ATLAS. Further, combining on-shell and off-shell measurements of the Higgs boson production, the observed (expected) value of the Higgs boson width was found to be  $4.3^{+2.7}_{-1.9} (4.1^{+3.5}_{-3.4})$  MeV.

#### D. Constraints on Higgs Self-Coupling

The trilinear self-coupling  $\lambda_{HHH}$  is a central parameter in testing the Higgs potential[27]. In the Standard Model, the Higgs boson self-coupling is predicted at the lowest order from values of the Higgs boson mass  $m_H$  and the Fermi constant  $G_F$ :

$$\lambda_{HHH} = \frac{m_H^2 G_F}{\sqrt{2}} \quad (88)$$

At the LHC, this self-interaction is most accessible through production of Higgs boson pairs, referred to as double-Higgs production or di-Higgs production (see Figure 47). By combining data from the most sensitive double Higgs channels,  $b\bar{b}\gamma\gamma$ ,  $b\bar{b}\tau^+\tau^-$ , and  $b\bar{b}b\bar{b}$ , using the complete Run-2 dataset at  $\sqrt{s} = 13$  TeV (integrated luminosity 126-139 fb $^{-1}$ , see Figure 48), constraints have been put on the coupling modifier as defined below Deviations are characterized by:

$$\kappa_\lambda = \frac{\lambda_{HHH}}{\lambda_{HHH}^{SM}} \quad (89)$$

An important point to note is that the single Higgs boson production cross section and branching ratios are modified, if the self-coupling deviates from SM predictions. Double-Higgs production processes, especially gluon-gluon fusion (ggF) and vector boson fusion (VBF), are particularly sensitive to  $\kappa_\lambda$ .

Using the  $\kappa$ -framework mentioned while discussing Higgs interactions, similar fits are carried out for  $\kappa_\lambda$ , by combining single Higgs-boson cross-section measurements of various decay channels. Finally, after assuming  $\kappa_\lambda$  as the only source of BSM physics, values outside  $-0.4 < \kappa_\lambda < 6.3$  are excluded at 95% CL. Assumptions about other  $\kappa$  involved may be loosened to get weaker, but less-model dependent constraints on  $\kappa_\lambda$ . Relevant constraints are shown in Figure 49.

#### CONCLUSION

In this paper, we have tried to review all essential properties of the Higgs boson from a holistic perspective, in-

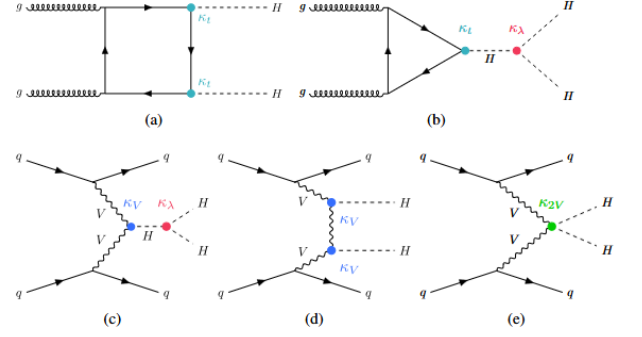


FIG. 47: Examples of leading-order Feynman diagrams for Higgs boson pair production: for ggF production, diagram (a) is proportional to the square of the top-quark Yukawa coupling, while diagram (b) is proportional to the product of the top-quark Yukawa coupling and the Higgs boson self-coupling. For VBF production, diagram (c) is proportional to the product of the coupling of the Higgs boson to the vector bosons and the self-coupling, diagram (d) to the square of the coupling to the vector bosons, and diagram (e) to the interaction between two vector bosons and two Higgs bosons.

Analysis channel	Integrated luminosity [fb $^{-1}$ ]
$HH \rightarrow b\bar{b}\gamma\gamma$	139
$HH \rightarrow b\bar{b}\tau^+\tau^-$	139
$HH \rightarrow b\bar{b}b\bar{b}$	126
$H \rightarrow \gamma\gamma$	139
$H \rightarrow ZZ^* \rightarrow 4\ell$	139
$H \rightarrow \tau^+\tau^-$	139
$H \rightarrow WW^* \rightarrow e\nu\mu\nu$ (ggF,VBF)	139
$H \rightarrow b\bar{b}$ (VH)	139
$H \rightarrow b\bar{b}$ (VBF)	126
$H \rightarrow b\bar{b}$ ( $t\bar{t}H$ )	139

FIG. 48: Decay channels used in single and double Higgs analyses to constrain self-coupling.

cluding theoretical formulations and experimental measurements. The utmost importance of the existence of the Higgs in the SM, as well as its properties and their measurement have been touched upon. We also included current development in Higgs physics in order to have an idea of the direction in which particle physics is evolving. We have aimed for maximum breadth accompanied by reasonable depth in exploring this topic. Certainly, some topics have not been touched upon that are extremely exciting (be it the proposed role of the Higgs particle in inflation, or the first search for tri-Higgs production in the LHC, to name a few). However, we believe this text will be a useful resource to anyone wishing to get introduced to the wonderful field of Higgs physics.

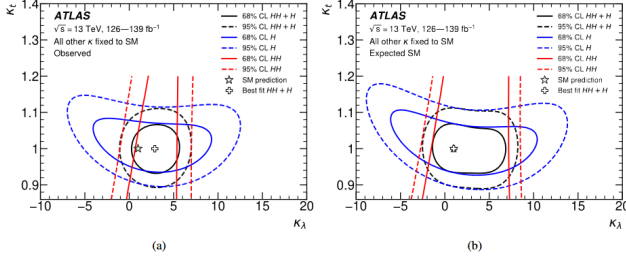


FIG. 49: Observed (a) and expected (b) constraints in the  $(\kappa_\lambda, \kappa_t)$  plane from single-Higgs (blue) and double-Higgs (red) analyses, and their combination (black). The solid (dashed) lines show the 68% (95%) CL contours. The double-Higgs contours are shown for values of  $\kappa_t$  smaller than 1.2. The observed constraint for the single and double-Higgs combination for  $\kappa_t$  values below unity is slightly less stringent than that for the single-Higgs fit alone due to the slightly higher best-fit value for this coupling modifier

## ACKNOWLEDGEMENTS

At the very outset, we thank Professor B. Anathanarayan, of the Centre of High Energy Physics, Indian Institute of Science, Bengaluru. We are grateful for the opportunity to explore a topic as dense and intricate as the Higgs. In preparing this report as well as our presentations, we learnt more than any of have could have expected to. We are also grateful to fellow batch mates in our course 'HE397: The Standard Model' for fruitful discussions.

We also extend our gratitude to members of the ATLAS experiment, especially for their excellent documentation and OpenData for Students and Research contributions, which was extremely useful in understanding relevant data analysis of ATLAS datasets. We hence, attach the link to a wonderful Jupyter notebook that analyzes OpenData, titled 'How to rediscover the Higgs' ([https://github.com/atlas-outreach-data-tools/notebooks-collection-opendata/tree/master/13-TeV-examples/uproot\\_python](https://github.com/atlas-outreach-data-tools/notebooks-collection-opendata/tree/master/13-TeV-examples/uproot_python)).

- [1] P. W. Higgs, Broken symmetries, massless particles and gauge fields, Phys. Lett. **12**, 132 (1964).
- [2] P. W. Higgs, Broken Symmetries and the Masses of Gauge Bosons, Phys. Rev. Lett. **13**, 508 (1964).
- [3] D. de Florian *et al.* (LHC Higgs Cross Section Working Group), Handbook of LHC Higgs Cross Sections: 4. Deciphering the Nature of the Higgs Sector **2/2017**, 10.23731/CYRM-2017-002 (2016), arXiv:1610.07922 [hep-ph].
- [4] R. Eichler and C. Grab, The Sindrum-I experiment, SciPost Physics Proceedings, 007 (2021).
- [5] G. Barr, P. Clarke, D. Coward, D. Cundy, *et al.*, Search for a neutral Higgs particle in the decay sequence  $KL0 \rightarrow \pi^0 H^0$  and  $H^0 \rightarrow e^+e^-$ , Physics Letters B **235**, 356 (1990).
- [6] D. Besson, J. Green, R. Namjoshi, F. Sannes, *et al.*, Search for monoenergetic photons from  $\Upsilon(1s) \rightarrow \gamma + X$ , Physical Review D **33**, 300 (1986).
- [7] M. M. Kado and C. G. Tully, The searches for higgs bosons at lep, Annual Review of Nuclear and Particle Science **52**, 65 (2002).
- [8] T. Aaltonen *et al.* (CDF, D0), Evidence for a particle produced in association with weak bosons and decaying to a bottom-antibottom quark pair in Higgs boson searches at the Tevatron, Phys. Rev. Lett. **109**, 071804 (2012), arXiv:1207.6436 [hep-ex].
- [9] Particle Data Group, P. A. Zyla, R. M. Barnett, J. Beringer, *et al.*, Review of particle physics, Progress of Theoretical and Experimental Physics **2020**, 083C01 (2020).
- [10] C. Vernieri, Search for the Higgs boson in the  $b\bar{b}$  - decay channel using the CMS detector, Nuclear and Particle Physics Proceedings **273–275**, 733 (2016).
- [11] F. Landua, The CERN accelerator complex layout in 2022. Complexe des accélérateurs du CERN en janvier 2022, (2022), general Photo.
- [12] G. Aad *et al.* (ATLAS), The ATLAS Experiment at the CERN Large Hadron Collider, JINST **3**, S08003.
- [13] The ATLAS Collaboration Software and Firmware, (2021).
- [14] G. Aad *et al.* (ATLAS), Combined search for the Standard Model Higgs boson using up to 4.9 fb $^{-1}$  of  $pp$  collision data at  $\sqrt{s} = 7$  TeV with the ATLAS detector at the LHC, Phys. Lett. B **710**, 49 (2012), arXiv:1202.1408 [hep-ex].
- [15] G. Aad *et al.* (ATLAS), Observation of a new particle in the search for the Standard Model Higgs boson with the ATLAS detector at the LHC, Phys. Lett. B **716**, 1 (2012), arXiv:1207.7214 [hep-ex].
- [16] G. Aad *et al.* (ATLAS, CMS), Combined Measurement of the Higgs Boson Mass in  $pp$  Collisions at  $\sqrt{s} = 7$  and 8 TeV with the ATLAS and CMS Experiments, Phys. Rev. Lett. **114**, 191803 (2015), arXiv:1503.07589 [hep-ex].
- [17] G. Aad *et al.* (ATLAS), A detailed map of Higgs boson interactions by the ATLAS experiment ten years after the discovery, Nature **607**, 52 (2022), [Erratum: Nature 612, E24 (2022)], arXiv:2207.00092 [hep-ex].
- [18] G. Aad *et al.* (ATLAS, CMS), Measurements of the Higgs boson production and decay rates and constraints on its couplings from a combined ATLAS and CMS analysis of the LHC  $pp$  collision data at  $\sqrt{s} = 7$  and 8 TeV, JHEP **08**, 045, arXiv:1606.02266 [hep-ex].
- [19] J. R. Andersen *et al.* (LHC Higgs Cross Section Working Group), Handbook of LHC Higgs Cross Sections: 3. Higgs Properties 10.5170/CERN-2013-004 (2013), arXiv:1307.1347 [hep-ph].
- [20] G. Aad *et al.* (ATLAS), Direct constraint on the Higgs-charm coupling from a search for Higgs boson decays into charm quarks with the ATLAS detector, Eur. Phys. J. C **82**, 717 (2022), arXiv:2201.11428 [hep-ex].
- [21] G. Aad *et al.* (ATLAS), Search for invisible Higgs-boson decays in events with vector-boson fusion signatures us-

- ing  $139 \text{ fb}^{-1}$  of proton-proton data recorded by the ATLAS experiment, JHEP **08**, 104, arXiv:2202.07953 [hep-ex].
- [22] M. R. Buckley and D. Goncalves, Boosting the Direct CP Measurement of the Higgs-Top Coupling, Phys. Rev. Lett. **116**, 091801 (2016), arXiv:1507.07926 [hep-ph].
  - [23] J. Brehmer, F. Kling, T. Plehn, and T. M. P. Tait, Better Higgs-CP Tests Through Information Geometry, Phys. Rev. D **97**, 095017 (2018), arXiv:1712.02350 [hep-ph].
  - [24] E. A. Smith (ATLAS TDAQ Group), The phase-1 upgrade of the ATLAS level-1 calorimeter trigger, PoS **EPS-HEP2021**, 754 (2022).
  - [25] G. Aad *et al.* (ATLAS), Measurement of the associated production of a top-antitop-quark pair and a Higgs boson decaying into a  $b\bar{b}$  pair in pp collisions at  $\sqrt{s} = 13 \text{ TeV}$  using the ATLAS detector at the LHC, Eur. Phys. J. C **85**, 210 (2025), arXiv:2407.10904 [hep-ex].
  - [26] G. Aad *et al.* (ATLAS), Measurement of off-shell Higgs boson production in the  $H^* \rightarrow ZZ \rightarrow 4\ell$  decay channel using a neural simulation-based inference technique in 13 TeV  $pp$  collisions with the ATLAS detector, (2024), arXiv:2412.01548 [hep-ex].
  - [27] G. Aad *et al.* (ATLAS), Constraints on the Higgs boson self-coupling from single- and double-Higgs production with the ATLAS detector using pp collisions at  $\sqrt{s}=13 \text{ TeV}$ , Phys. Lett. B **843**, 137745 (2023), arXiv:2211.01216 [hep-ex].
  - [28] C. D. F. Collaboration and D. Collaboration, Evidence for a particle produced in association with weak bosons and decaying to a bottom-antibottom quark pair in Higgs boson searches at the Tevatron (2012).
  - [29] S. Dawson, C. Englert, and T. Plehn, Higgs Physics: It ain't over till it's over (2019).
  - [30] S. Giagu, Latest and near-future physics highlights from the atlas experiment (2024).
  - [31] A. J. M. Muijs, *Tau pair production above the Z resonance*, Other thesis (2001).
  - [32] L. H. W. Group, Lephiggs.
  - [33] Searches for new particles in Z decays using the ALEPH detector, Physics Reports **216**, 253 (1992).
  - [34] C. G. Tully, *Elementary Particle Physics in a Nutshell*, In a Nutshell (Princeton university press, Princeton, 2011).
  - [35] P. Langacker, *The standard model and beyond* (2010).